CHAPTER 2

BACKGROUND

Microstrip patch antennas can easily be made to conform to cylindrical surfaces to provide low profile omnidirectional arrays. A specified array pattern can also be obtained by configuring the geometries of the elements, the array and the cylinder. For a design procedure, the radiation patterns of the cylindrical patch elements and the array are needed. The cavity model is well suited to analyse cylindrical patches etched on thin substrates and to demonstrate the characteristics of these patch antennas. Two linear polarisations with different radiation characteristics are available when utilising cylindrical patches. In the first part of this chapter, the characteristics of the radiated fields for both polarisations will be discussed. The radiated fields will also be compared for different substrates and cylinder radii.

Due to the cylindrical configuration of the microstrip patch array, the array is classified as a cylindrical array. An introduction to cylindrical arrays and equally spaced cylindrical arrays, will be given. When the elements are equally spaced around the circumference of the array, the elements can be excited by using phase-sequence excitations. The orthogonal set of excitation vectors resulting from these phase-sequences may be implemented in a pattern synthesis method to obtain an optimal set of excitations for a required radiation pattern.

The objective in this thesis is to provide an omnidirectional radiation pattern with one or more nulls at specified angle locations to suppress directional interferences. Different techniques have been presented which perform null beam forming or null pattern synthesis [41,43–55]. In null beam forming, additional nulls are introduced in the beam

pattern, while null pattern synthesis provide omnidirectional coverage with directional nulls. In this chapter, a discussion on various null synthesis techniques for omnidirectional patterns will be given. These methods determine the element excitations which provide the required array radiation pattern.

The element excitations are applied to the array by setting either the element currents or voltages proportional to the excitations. When the mutual coupling between the antenna elements in the array is not taken into account during the computation of the excitations, the resulting radiation pattern may be distorted [53, 72–74]. Not only does the coupling deform the array imbedded radiation patterns of the individual elements, but also modifies the active impedances at the element ports. Consequently, a technique to compensate for the mutual coupling has to be implemented to obtain the desired array radiation pattern. Different techniques to compensate for the mutual coupling during the synthesis process, will also be discussed.

2.1 Characteristics of a cylindrical microstrip patch

Utilising the cavity model for the cylindrical patch antenna, the characteristics of the patches can be studied. These antennas may be used in two linear polarisations with different radiation characteristics, which will be discussed in the following paragraphs.

2.1.1 Cavity model for cylindrical microstrip patches

The geometry of a typical cylindrical microstrip patch antenna is shown in Figure 2.1. $2b$ and $2\theta_0$ define the dimensions of the patch in the z and ϕ directions, respectively. ϕ_0 indicates the ϕ-position of the patch, while a and h define the radius of the cylinder and height of the substrate, respectively. The position of the coaxial probe feed is indicated by z_f and ϕ_f.

One model for the cylindrical patch can be found by regarding the region underneath the patch as a cavity bounded by four magnetic walls and two electric walls [5, 7]. The E-field in the cavity has only a ρ component, which is independent of ρ if the substrate is thin ($h \ll a$). When the coaxial probe feed is modeled by a current density, with

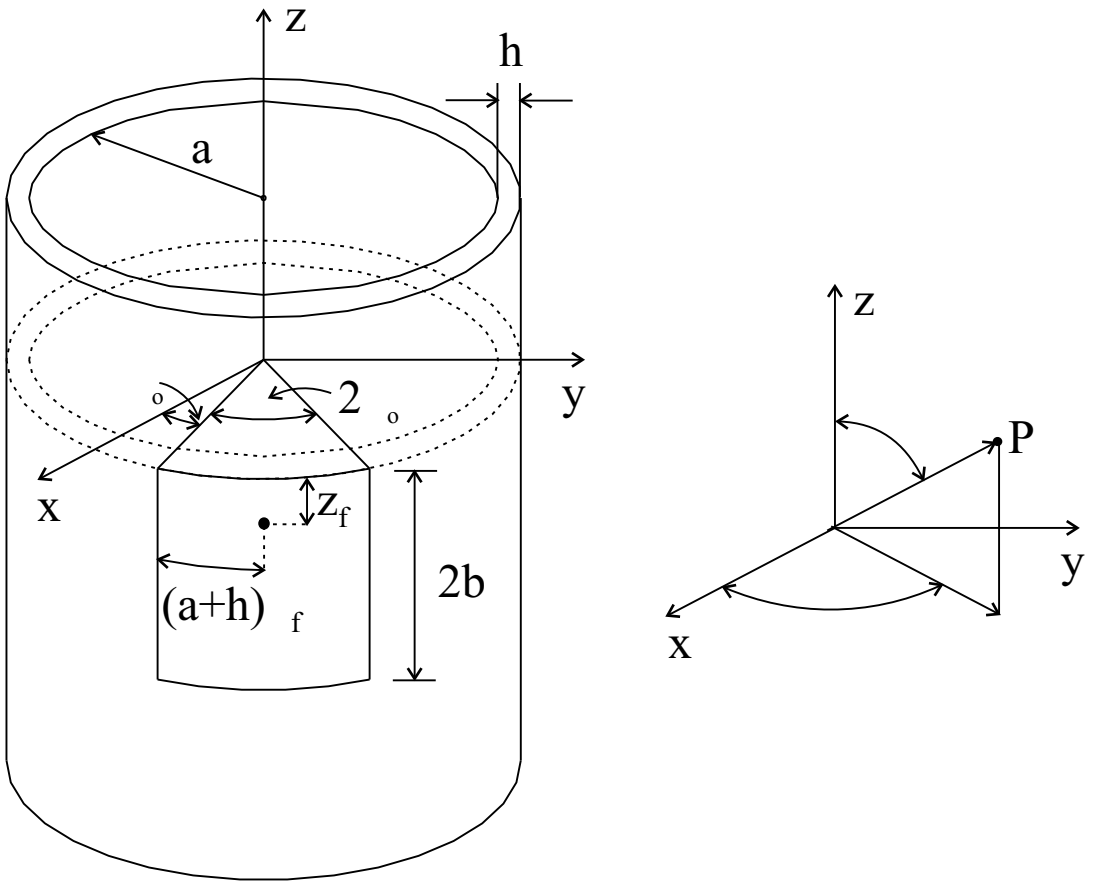

Figure 2.1: Geometry of cylindrical microstrip patch antenna

an effective width w, the field in the cavity can be found by a summation over all the cavity modes [13]:

$$E_\rho = j\omega\mu_0 \sum_{m,n} C_{mn} \cos\left[\frac{m\pi}{2\theta_0}(\phi - \phi_0)\right] \cos\left[\frac{n\pi z}{2b}\right], \tag{2.1}$$

where m and n are the mode indexes. The modal amplitudes C_{mn} are defined as:

$$C_{mn} = \frac{w}{k_{eff}^2 - k_{mn}^2} \frac{\Delta_m \Delta_n}{4(a+h)b\theta_0} \cos\left[\frac{m\pi\phi_f}{2\theta_0}\right] \cos\left[\frac{n\pi z_f}{2b}\right] \operatorname{sinc}\left[\frac{m\pi w}{4(a+h)\theta_0}\right], \tag{2.2}$$

where

$$\Delta_k = \begin{cases} 1, & k = 0 \\ 2, & k \neq 0 \end{cases}, \tag{2.3}$$

$$k_{mn} = \sqrt{\left(\frac{m\pi}{2(a+h)\theta_0}\right)^2 + \left(\frac{n\pi}{2b}\right)^2}, \tag{2.4}$$

$$k_{eff} = k_0\sqrt{\varepsilon_r(1 - j\delta_{eff})}, \tag{2.5}$$

$$\text{sinc}(x) = \sin(x)/x, \tag{2.6}$$

and

$$k_0 = \omega\sqrt{\mu_0\varepsilon_0}. \tag{2.7}$$

μ_0 and ε_0 are the permeability and permittivity of free space, respectively. The radial frequency and relative permittivity of the substrate are presented by ω and ε_r, respectively. The effective loss tangent δ_{eff} represents all the losses in the cavity. The radiation losses, the losses due to the finite conductivity of the conductor and the losses in the substrate and through surface waves can be estimated using the method described in [6]. The modal resonant frequency is given by:

$$f_{mn} = \frac{c}{2\sqrt{\varepsilon_r}}\sqrt{\left(\frac{m\pi}{2(a+h)\theta_0}\right)^2 + \left(\frac{n\pi}{2b}\right)^2}. \tag{2.8}$$

When the dimensions $2(a+h)\theta_0$ and $2b$ of the patch are fixed, Equation 2.8 indicates that the resonant frequency f_{mn} is independent of the curvature. This assumption is only valid for thin substrates with $h \ll a$ [7].

2.1.2 Radiated fields

The four walls of the lossy cavity in the cavity model are considered as the radiating apertures. Along each wall an equivalent magnetic current can be found from:

$$\bar{M} = E_\rho\hat{\rho} \times \hat{n}, \tag{2.9}$$

where E_ρ is given by Equation 2.1. These radiating walls are also referred to as radiating slots. For these magnetic currents radiating in the vicinity of an infinitely long cylindrical surface, the far zone radiation field may be obtained using the expressions

presented in [98]. The resulting components of the far zone electric fields for each cavity mode are given by [13]:

$$E_{\theta,mn}(r,\phi,\theta) = \frac{E_0 h}{2\pi^2 \sin\theta}\frac{e^{-jk_0 r}}{r}\left[1-(-1)^n e^{-j2k_0 b\cos\theta}\right] \cdot \sum_{p=-\infty}^{\infty}\frac{j^{p+1}e^{jp(\phi-\phi_0)}I(\theta_0,m,-p)}{H_p^{(2)}(k_0 a\sin\theta)}, \tag{2.10}$$

and

$$\begin{aligned} E_{\phi,mn}(r,\phi,\theta) = {} & -j\frac{E_0 h}{2\pi^2 a}\frac{e^{-jk_0 r}}{r}I(b,n,-k_0\cos\theta) \\ & \cdot\sum_{p=-\infty}^{\infty}\frac{j^{p+1}e^{jp(\phi-\phi_0)}}{H_p^{(2)\prime}(k_0 a\sin\theta)}\left[1-(-1)^m e^{-j2p\theta_0}\right] \\ & -j\frac{E_0 h}{2\pi^2 a}\frac{e^{-jk_0 r}}{r}\frac{\cos\theta}{k_0\sin^2\theta}\left[1-(-1)^n e^{-j2k_0 b\cos\theta}\right] \\ & \cdot\sum_{p=-\infty}^{\infty}\frac{j^{p+1}pe^{jp(\phi-\phi_0)}I(\theta_0,m,-p)}{H_p^{(2)\prime}(k_0 a\sin\theta)}, \end{aligned} \tag{2.11}$$

where

$$I(b,n,u) = \int_{-2b}^{0}\cos\left(\frac{n\pi z}{2b}\right)e^{-juz}dz, \tag{2.12}$$

and

$$I(\theta_0,m,-p) = \int_{0}^{2\theta_0}\cos\left(\frac{m\pi\phi}{2\theta_0}\right)e^{-jp\phi}d\phi. \tag{2.13}$$

The total radiated field is obtained by a summation over all the cavity modes m,n. The infinite summations in Equations 2.10 and 2.11 are summations over the cylindrical modes in which the fields have been expanded. The number of cylindrical modes needed for convergence depends on the radius of the cylinder and the angle θ, but is usually less than $2ka$ [11]. For θ-angles close to the cylinder axis, only a small number of terms are required.

2.1.3 Axial polarisation

The two slots of the cavity, oriented along the axis of the cylinder, are referred to as axial slots, while the other two slots, oriented along the circumference of the cylinder, are called circumferential slots. The patch antenna is axially polarised when fed symmetrically in ϕ, as shown in Figure 2.2. The dominant mode in the cavity will be the mode m=0, n=1 (TM_{01}). The two circumferential slots are excited equally in phase and amplitude, while the two axial slots are excited 180° out of phase. The next two higher order modes will be the TM_{20} and TM_{21} modes, with the TM_{20} mode mainly contributing to the cross-polar radiation. The TM_{21} mode contributes weakly to both the co-polar and cross-polar radiation. The TM_{01} mode itself gives rise to the E_θ co-polar radiation with no cross-polar radiation in the symmetry planes. Since the other higher modes are excited much weaker, most cross-polar radiation originate from the TM_{20} mode. A small displacement in ϕ_f will cause the TM_{10} to be excited, which will result in a higher cross-polarisation level [11]. Special care must be taken when feeding square patches, since the TM_{01} and TM_{10} will have the same resonant frequency.

2.1.4 Circumferential polarisation

The TM_{10} mode is the dominant mode for a circumferentially polarised patch, since it is fed symmetrically in z, as shown in Figure 2.3. The E_ϕ co-polar radiation is given by the two axial slots excited in phase. The two higher order modes contributing the most to the radiation are the TM_{02} and TM_{12} modes, with the cross-polarisation level mainly determined by the radiation from the TM_{02} mode.

2.1.5 Characteristics of the radiation patterns

The radiation pattern of a cylindrical patch depends on the geometries of the cylinder (a) and the patch (θ_0,b), as well as the characteristics of the substrate (h,ε_r). A comparison of the radiation patterns for patches with different substrates is shown in Figures 2.4 to 2.7. The radiation patterns were determined using the cavity model (Equations 2.10 and 2.11) at 1.8 GHz.

An air substrate was used for the first patch, with dimensions L=73.6 mm and W=76 mm.

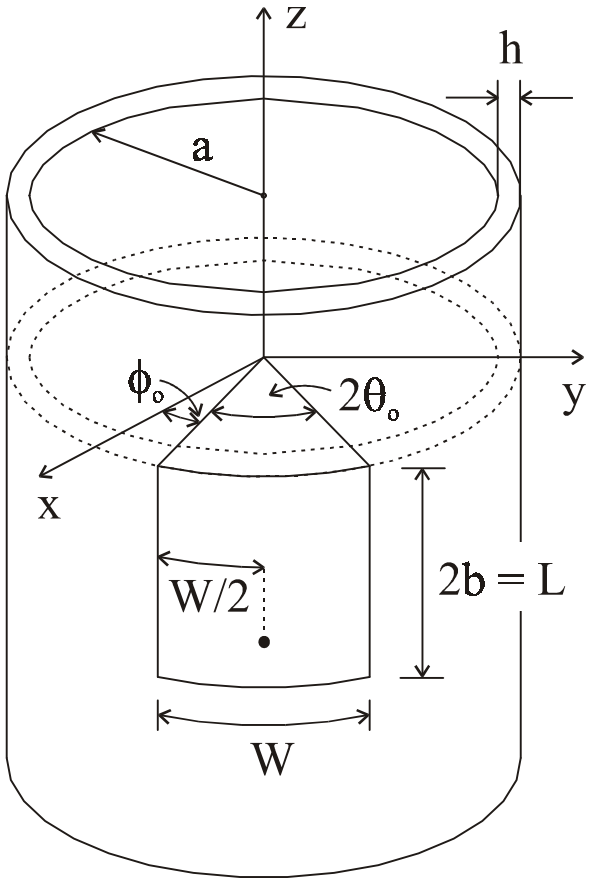

Figure 2.2: Geometry of an axial polarised patch antenna

The dimensions for the second patch were L=38.3 mm and W=42 mm and the substrate had an ε_r of 4.4. For both patches, h was 1.6 mm and $\phi_0 = 90° - \theta_0$. A cylinder, with a=131 mm, was used and the radiation patterns of the two patches were compared for both polarisations. The radiated relative power density in the E-plane and H-plane, for the patches used in the circumferential polarisation, is shown Figures 2.4 and 2.5, respectively. The patch, with an air substrate, radiates a co-polar component (P_ϕ) with a higher directivity and a lower back lobe level in both the E-plane and H-plane. The cross-polarisation level in the H-plane is also higher when using the air substrate.

For the two patches used in the axial polarisation, Figures 2.6 and 2.7 show the radiated relative power density in the H-plane and E-plane, respectively. The co-polar component (P_θ) of the air substrate patch show again a higher directivity and lower back lobe level in both principal planes. The cross-polar component in the H-plane is also higher for this patch.

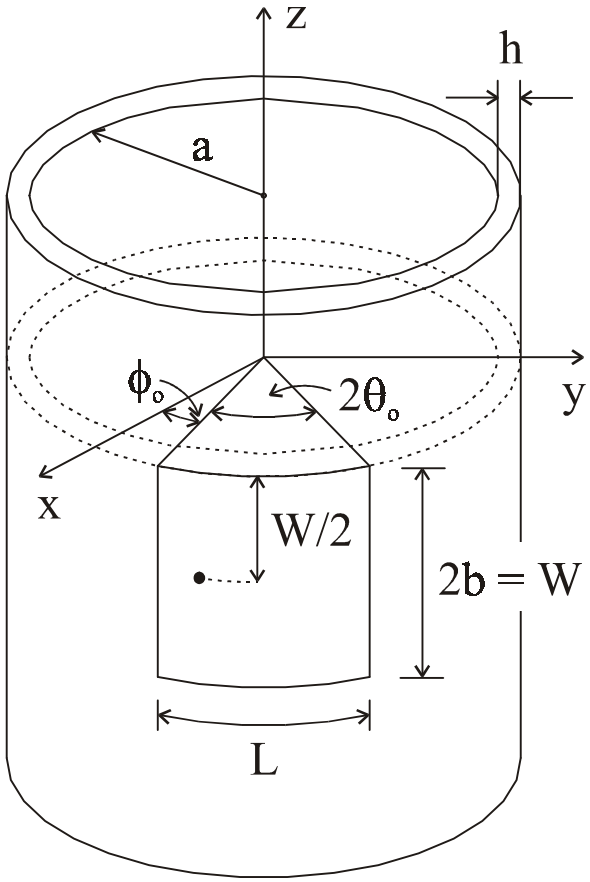

Figure 2.3: Geometry of a circumferentially polarised patch antenna

When comparing Figures 2.4 and 2.6, it is seen that the back lobe level of the axially polarised patches is much less (below -40 dB) than the back lobe level of the circumferentially polarised patches. Depending on the permittivity of the substrate, the main lobe of an axial polarised patch is either broader or narrower than the main lobe of a circumferentially polarised patch. With $\varepsilon_r = 1$, the main lobe is broader for the circumferentially polarised patch, and for the case where $\varepsilon_r = 4.4$, the axial polarised patch has the broader main beam.

In Figure 2.7 it is observed that the level of radiation increases near the axis of the cylinder. In the cavity model, the axial slots are not radiating in this cut ($\phi = 90°$) of the radiation pattern and therefore these high levels of radiation are not suppressed. In reality, the axial slots do radiate close to the cylinder axis to give the radiation pattern a finite value. In the cavity model, it is also assumed that the cylinder has an infinite length. For the radiation measurements to be comparable to the simulations using this model, the cylinder has to be at least a few wavelengths long.

The cylindrical patch with the air substrate was also simulated on a cylinder with a different radius (a=265 mm) to show the effect of curvature. Figures 2.8 and 2.9 compare the relative power density patterns of the circumferential polarisation for the two different radii in the E-plane and H-plane, respectively. The back lobe level decreases when using the larger radius, while the main lobe is only slightly effected in both principle planes. The influence of the curvature is less when using the cylindrical patch in the axial polarisation. The H-plane and E-plane relative power density patterns for the axial polarisation are compared for the two radii in Figures 2.10 and 2.11, respectively. A small decrease in the back lobe level in the H-plane is observed, while the effect of the decreased curvature on the main lobe is insignificant in both principle planes. The cross-polarisation levels for both polarisations appear to be almost unaffected by the decrease in curvature.

2.2 Cylindrical array pattern

The geometry of a typical cylindrical array can be seen in Figure 2.12. Each array element is placed on the circumference of the array at (x_n, y_n), where $n = 1 \ldots N$. The contribution of the n-th element to the far-field in direction (ϕ, θ) can be written as:

$$e\left(r, \phi, \theta\right) = E_n(r, \phi, \theta) e^{jk_0(x_n \sin\theta\cos\phi + y_n \sin\theta\sin\phi)}, \tag{2.14}$$

using the origin of the coordinate system as the reference point. $E_n(r, \phi, \theta)$ represent the co-polarised far-zone electric field of the n-th element with respect to its phase reference. The radiated electric field of the elements is influenced by the structure on which it is mounted, e.g. a conducting cylinder or mast, and must therefore be included when computing element electric fields. The total co-polarised far-zone electric field $E_{TOT}(r, \phi, \theta)$ of the array is found by superposition of the element electric fields:

$$E_{TOT}\left(r, \phi, \theta\right) = \sum_{n=1}^{N} a_n E_n(r, \phi, \theta) e^{jk_0(x_n \sin\theta\cos\phi + y_n \sin\theta\sin\phi)}, \tag{2.15}$$

where a_n denotes the relative complex excitation (amplitude as well as phase) of the n-th element.

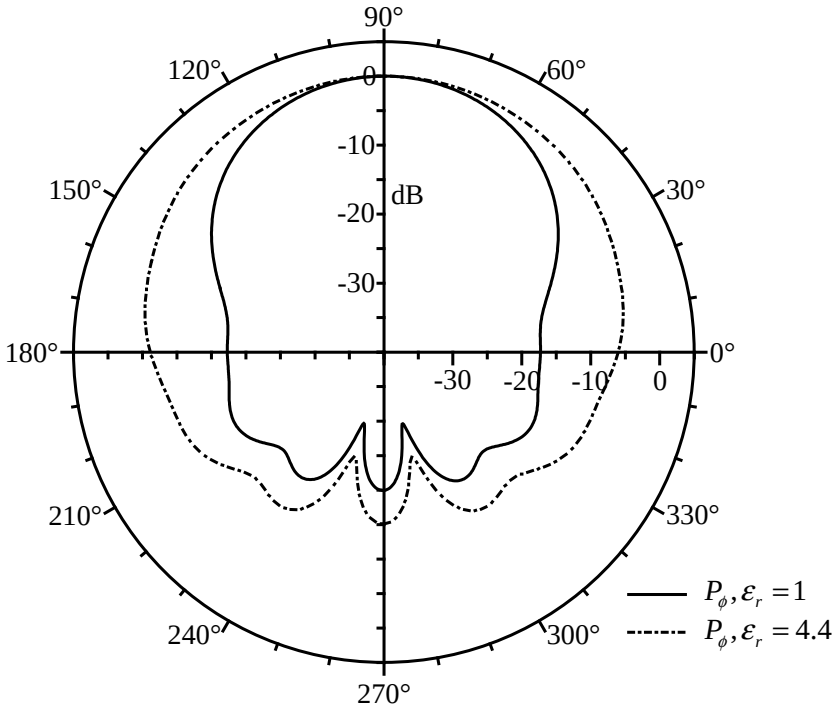

Figure 2.4: Radiated relative power density at $\theta = 90°$ (E-plane) for circumferentially polarised patches with $\varepsilon_r = 1$ and $\varepsilon_r = 4.4$

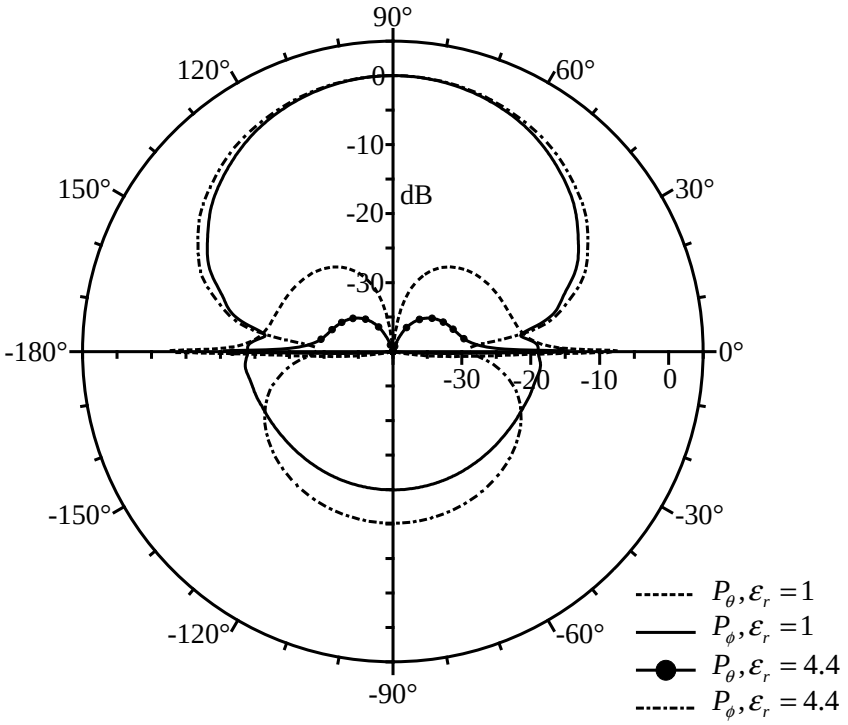

Figure 2.5: Radiated relative power density at $\phi = 90°$ (H-plane) for circumferentially polarised patches with $\varepsilon_r = 1$ and $\varepsilon_r = 4.4$

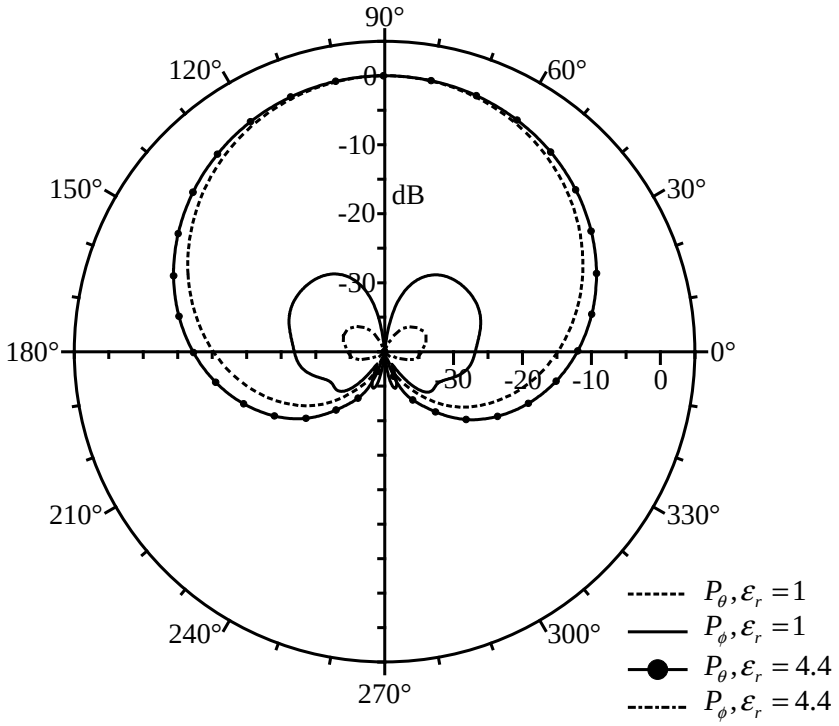

Figure 2.6: Radiated relative power density at $\theta = 90°$ (H-plane) for axial polarised patches with $\varepsilon_r = 1$ and $\varepsilon_r = 4.4$

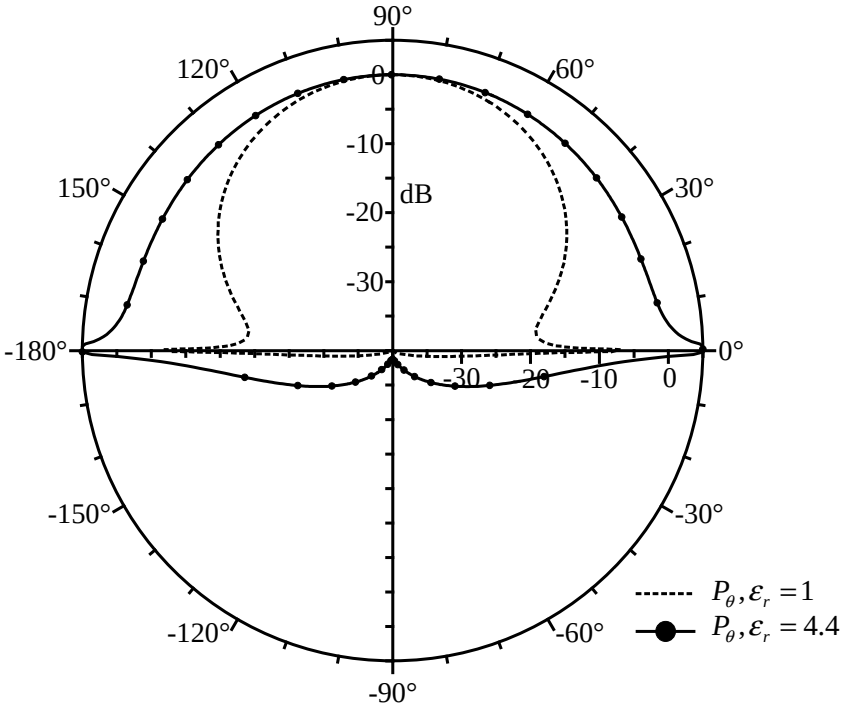

Figure 2.7: Radiated relative power density at $\phi = 90°$ (E-plane) for axial polarised patches with $\varepsilon_r = 1$ and $\varepsilon_r = 4.4$

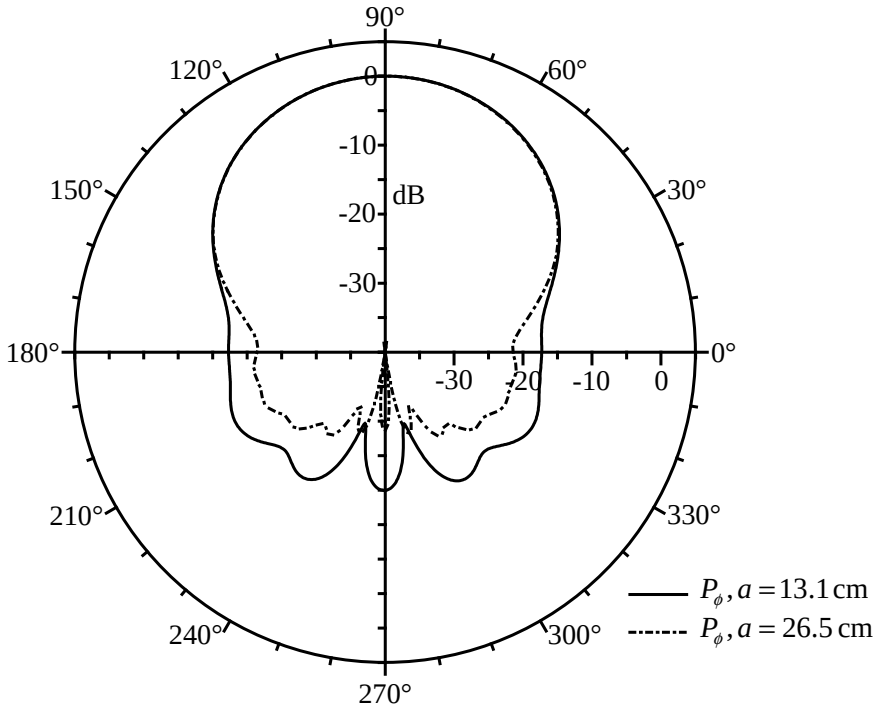

Figure 2.8: Radiated relative power density at $\theta = 90°$ (E-plane) for circumferentially polarised patches mounted on cylinders with a=13.1 cm and a=26.5 cm, respectively.

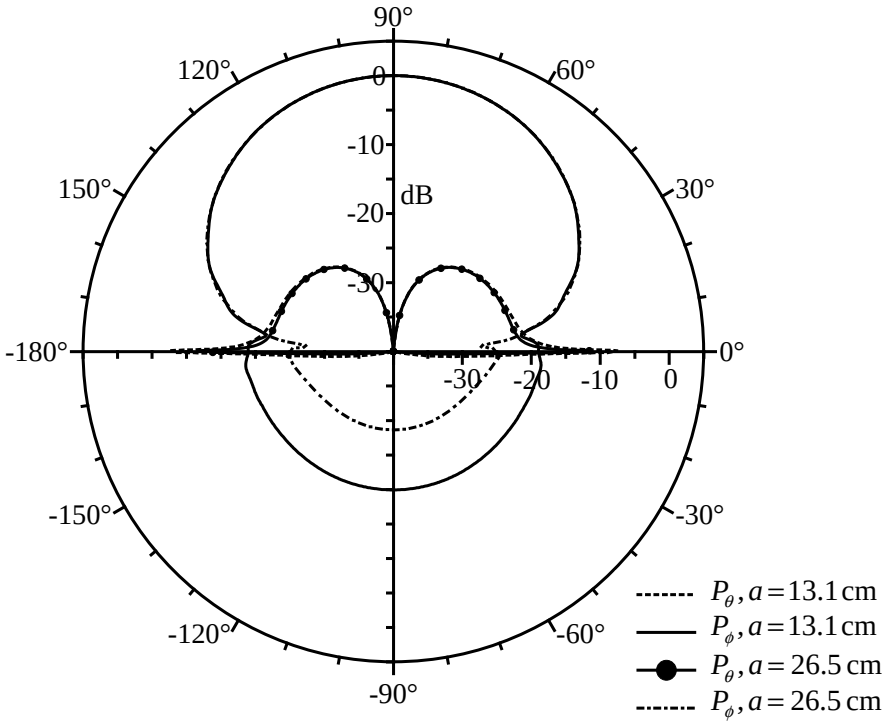

Figure 2.9: Radiated relative power density at $\phi = 90°$ (H-plane) for circumferentially polarised patches mounted on cylinders with a=13.1 cm and a=26.5 cm, respectively.

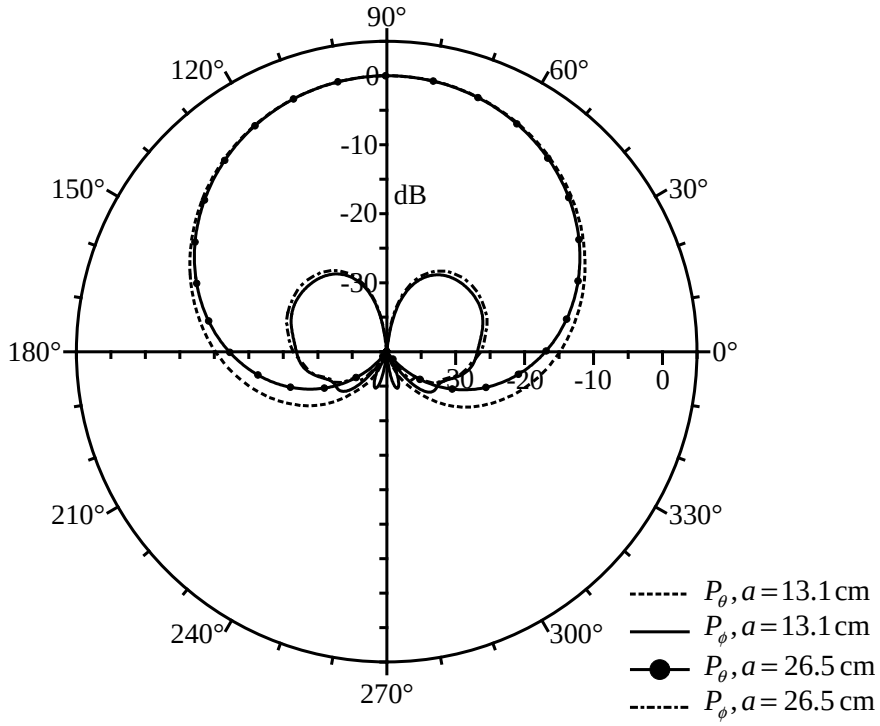

Figure 2.10: Radiated relative power density at $\theta = 90°$ (H-plane) for axial polarised patches mounted on cylinders with a=13.1 cm and a=26.5 cm, respectively.

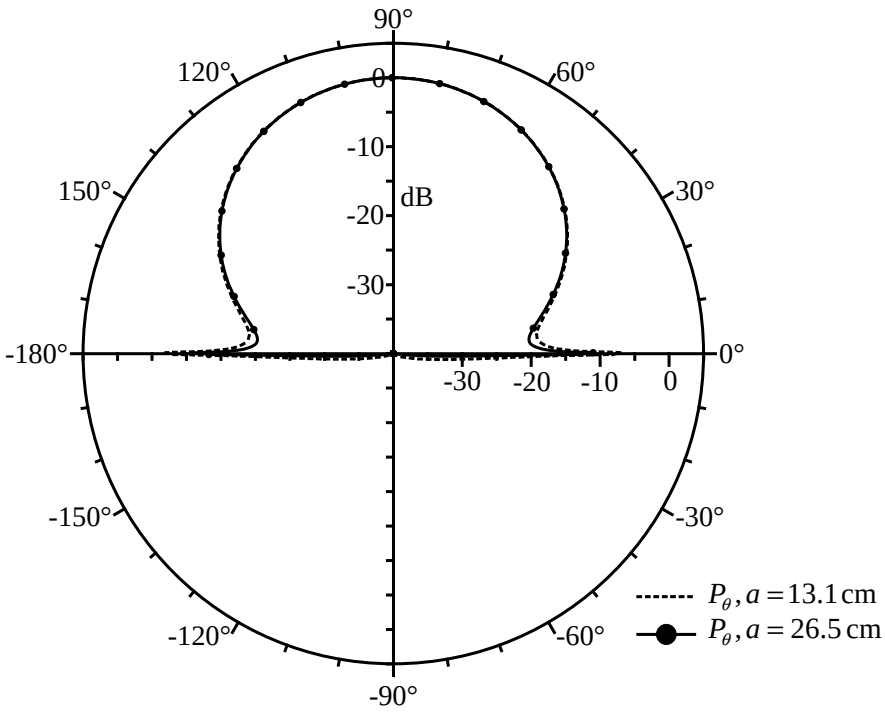

Figure 2.11: Radiated relative power density at $\phi = 90°$ (E-plane) for axial polarised patches mounted on cylinders with a=13.1 cm and a=26.5 cm, respectively.

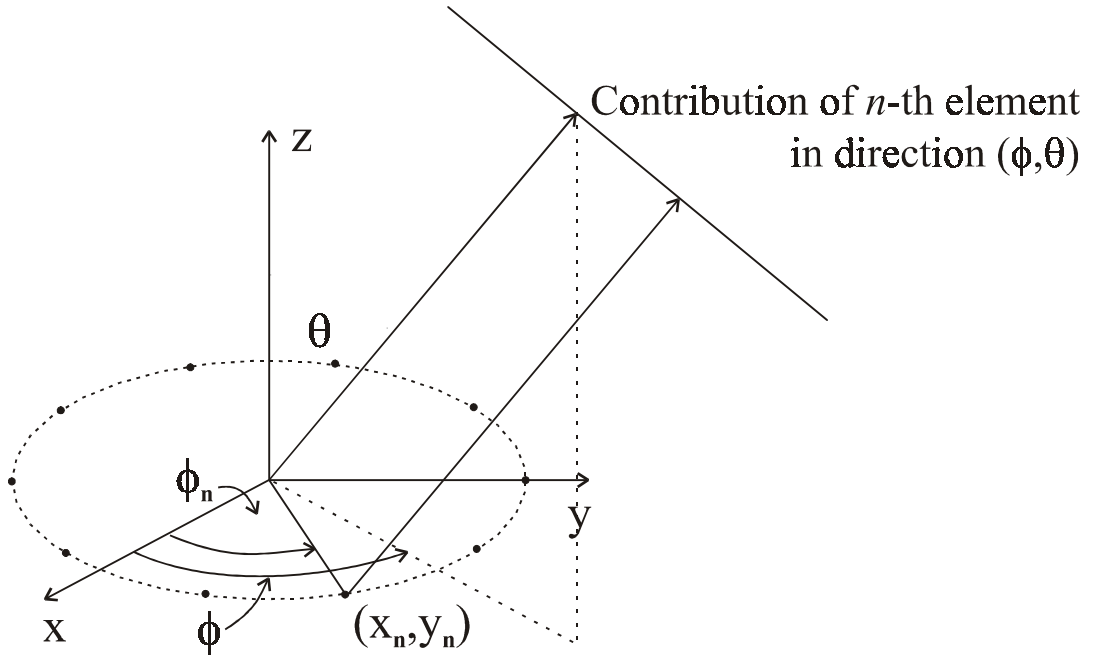

Figure 2.12: Geometry of a cylindrical array

The far-field radiation pattern of the array may then be written as:

$$F(\phi,\theta) = \sum_{n=1}^{N} a_n E_n(\phi,\theta) e^{jk_0(x_n \sin\theta\cos\phi + y_n \sin\theta\sin\phi)}, \tag{2.16}$$

with $E_n(\phi,\theta)$ being the far-field radiation pattern of the n-th element.

When only the cross-section of the radiation pattern in the plane of the cylindrical array ($\theta = 90°$) is considered, Equation 2.16 reduces to:

$$F(\phi) = \sum_{n=1}^{N} a_n E_n(\phi) e^{jk_0(x_n \cos\phi + y_n \sin\phi)}, \tag{2.17}$$

where $E_n(\phi)$ is the n-th element's radiation pattern in the $\theta = 90°$ plane. The array radiation pattern may be evaluated in vector form [57] :

$$\mathbf{F} = \mathbf{BA}. \tag{2.18}$$

The radiation pattern vector $\mathbf{F}$ is given as:

$$\mathbf{F} = [f_1, f_2, \ldots, f_q, \ldots, f_Q]^T, \tag{2.19}$$

where f_q is the value of the radiation pattern in the ϕ_q-direction for a total number of Q field points. $\mathbf{A}$ is the excitation vector:

$$\mathbf{A} = [a_1, a_2, \ldots, a_n, \ldots, a_N]^T, \tag{2.20}$$

while $\mathbf{B}$ is defined as the radiation matrix. The b_{nq}-th element of $\mathbf{B}$ is the contribution of the n-th antenna element to the radiation pattern in the q-th direction:

$$b_{nq} = a_n E_n(\phi_q) e^{jk_0(x_n \cos\phi_q + y_n \sin\phi_q)}. \tag{2.21}$$

When all the antenna elements have the same radiation pattern $E(\phi)$, polarisation properties and pointing direction, the array radiation pattern may be written as:

$$F(\phi) = E(\phi) \cdot \left[\sum_{n=1}^{N} a_n e^{jk_0(x_n \cos\phi + y_n \sin\phi)} \right]. \tag{2.22}$$

From this radiation pattern an array factor can be extracted:

$$AF(\phi) = \sum_{n=1}^{N} a_n e^{jk_0(x_n \cos\phi + y_n \sin\phi)}, \tag{2.23}$$

which is the radiation pattern of an array of isotropic point sources located at the phase centres of the original elements and with excitations equal to the original element excitations. Isotropic point sources are fictitious antenna elements that radiate an equal amount of energy in all directions.

2.2.1 Equally spaced cylindrical arrays

The geometry of an equally spaced cylindrical array in the xy-plane ($\theta = 90°$) is shown in Figure 2.13. The n-th is located at the angle:

$$\phi_n = \frac{2\pi n}{N}. \tag{2.24}$$

The far-field array factor for an equally spaced array with elements identical in radiation pattern, is given by [41]:

$$\begin{aligned} AF(\phi) &= \sum_{n=1}^{N} a_n e^{jk_0 R\cos(\phi - \phi_n)} \\ &= \sum_{n=1}^{N} a_n e^{jk_0 R\cos\left(\phi - \frac{2\pi n}{N}\right)}, \end{aligned} \tag{2.25}$$

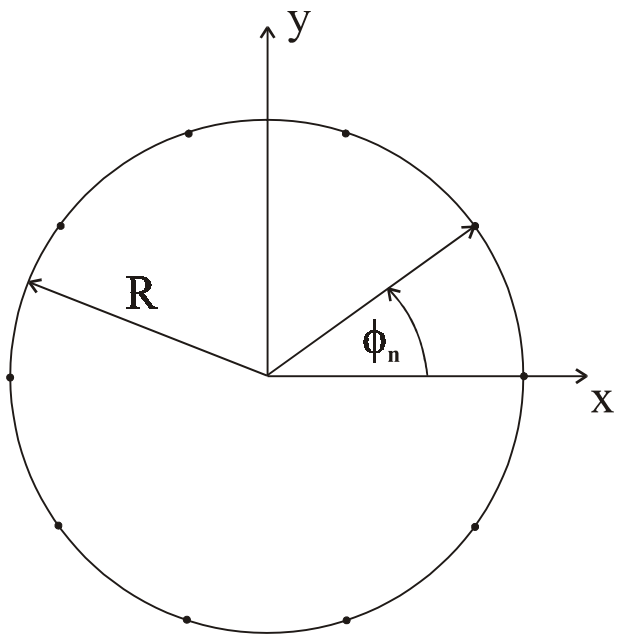

Figure 2.13: Geometry of an equally spaced cylindrical array in the xy-plane

where the radius of the cylindrical array is equal to R.

These equally spaced arrays are very suitable to form omnidirectional radiation patterns. It is evident from symmetry that any constant-amplitude excitation with an integral number of closed cycles of phase variations around the array will produce an omnidirectional pattern. Such an excitation is called a phase-sequence excitation [41]. There will, however, always be a ripple in the array radiation pattern which will depend on the distances between the antenna elements and on the element radiation patterns [42] . The m-th sequence excitation is one in which the total phase change around the array is $m2\pi$, with m an integer. For $m = 0$, all the elements are fed in phase, which also gives an omnidirectional array pattern. Consequently, the excitation of the n-th element for the m-th sequence excitation is:

$$a_{nm} = e^{j\frac{2\pi mn}{N}}. \tag{2.26}$$

The element excitations for a sequence excitation of order $m + N$ will be the same as for the m-th sequence excitation, since sine and cosine functions are periodical with 2π. Using Equation 2.26 it can also be shown that the element excitations of the $(m + p)$-th sequence excitation are orthogonal to those of the m-th sequence excitation, with $p \neq N$. The sequence excitations of orders 0 to $N-1$ thus form a complete orthogonal base for the space of element excitations. Every possible array pattern can therefore be

realised by the superposition of N sequence excitations. The transformations between the vectors of element excitations and sequence excitations are given by:

$$a_n = \sum_{m=0}^{N-1} s_m e^{j\frac{2\pi mn}{N}}, \tag{2.27}$$

and

$$s_m = \frac{1}{N}\sum_{n=0}^{N-1} a_n e^{-j\frac{2\pi mn}{N}}. \tag{2.28}$$

Equation 2.27 and Equation 2.28 can be seen as a discrete Fourier transform (DFT) and an inverse discrete Fourier transform (IDFT), respectively. Subsequently, the far-field array factor of the m-th sequence excitation can be expressed as:

$$AF_m(\phi) = \sum_{n=0}^{N-1} s_m e^{j\frac{2\pi mn}{N}} e^{jk_0 R\cos\left(\phi-\frac{2\pi n}{N}\right)}. \tag{2.29}$$

Since the element excitations are superpositions of N sequence excitations, the array factor becomes:

$$AF(\phi) = \sum_{m=0}^{N-1}\sum_{n=0}^{N-1} s_m e^{j\frac{2\pi mn}{N}} e^{jk_0 R\cos\left(\phi-\frac{2\pi n}{N}\right)}. \tag{2.30}$$

When the resulting array pattern has a constant amplitude and linear phase, it is called a phase mode [44]. The order of the phase mode is determined by the number of phase variations over 2π. A phase mode of order m is:

$$p_m(\phi) = e^{jm\phi}. \tag{2.31}$$

The zero order phase mode has constant amplitude and phase, while the negative order phase modes indicate a reverse variation of phase change with angle. For small inter-element spacings, the array can be approximated by a continuous source of radiation and the array factor can then be expressed as [43]:

$$AF(\phi) = N\sum_{m=-m_{max}}^{m=m_{max}} j^m s_m J_m(k_0 R) e^{jm\phi}, \tag{2.32}$$

where $J_m(x)$ is the Bessel function of the first kind of order m and $m_{max} < N/2$. This array factor is a superposition of N scaled phase modes with $-N/2 < m < N/2$. Consequently, a pattern caused by a sequence excitation of order m is a good approximation for a phase mode of the same order if the array radius is small.

2.3 Null synthesis techniques

Various null synthesis techniques for omnidirectional patterns have been presented [41, 43–55]. These techniques utilise different characteristics of a cylindrical array to obtain a null at the desired angle location. Some use the sequence excitations, phase modes or the orthogonal base of realisable array patterns, while others utilise pattern search techniques. A short overview of these techniques will be given after defining some null synthesis parameters.

2.3.1 Definitions of parameters in null synthesis

The definitions describing the omnidirectional radiation pattern with a null, differ from conventional beam forming parameters such as beam width and side lobe levels. Illustrations of the definitions used to characterise the null pattern, are given in Figure 2.14. The gain ripple (in dB) is defined as the ratio between the maximum and minimum level in the omniregion. The angular distance between the two points, 10 dB below the maximum, is defined as the null width. The null depth is given by the ratio of the radiation intensity in the direction of the null and the maximum, which is also an indication of the suppression level of the interference. For null depths smaller than 10 dB, another appropriate level may be defined at which the null width is measured. The definition of gain ripple is only valid if the value of the ripple is below this null width definition level.

2.3.2 Superposition of sequence excitations

The superposition of two sequence excitations to produce a null in an omnidirectional radiation pattern, was presented by Davies and Rizk [44]. A zero crossing null, where the radiation pattern show an abrupt phase reversal across the angle position of the null, was produced. The two phase modes, which had the same amplitude, but were 180° out of phase in the direction of the null, were utilised. The difference in the orders of the two modes had to be exactly one to avoid any other abrupt phase reversals. The authors consequently employed the zero and first order sequence excitations. The

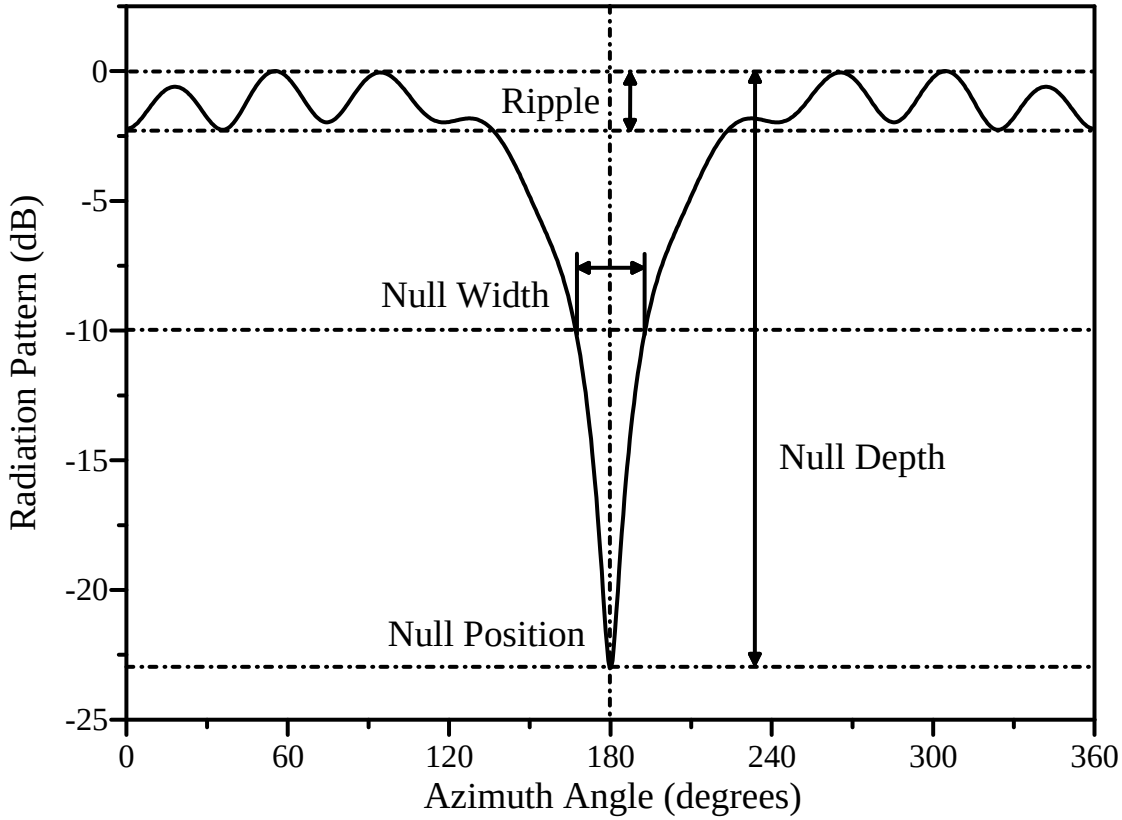

Figure 2.14: Definitions of parameters used to characterise null forming

excitations of the n-th element was:

$$a_n = e^{j2\pi\frac{n}{N}} + Ae^{j\phi_p}. \tag{2.33}$$

The levels of excitation of the two modes were made equal by means of an attenuator A, and the direction of the null was controlled by a phase shifter ϕ_p. Acceptable null depths are obtainable if the number of elements and the radius of the array is kept small. If the inter-element spacing is not kept small, the two modes do not exactly cancel each other. This will lead to finite null depths and errors in the direction of the null. This technique produced very wide nulls as the amplitude of the radiation pattern falls monotonically from the maximum towards the null.

As an extension of this technique, the above authors also proposed the superposition of a third sequence excitation to reduce the null width. A dipole type or figure-of-eight pattern was superposed to the original pattern. This type of pattern was produced by the sequence excitations of orders 1 and -1 and has two zero crossing nulls. One of the two nulls was made to coincide with the original null. The complete excitation vector

was given by:

$$a_n = Ae^{j\phi_p} + (B+1)e^{j2\pi\frac{n}{N}} + Be^{\left(j2\phi_p - j2\pi\frac{n}{N}\right)}. \tag{2.34}$$

The decrease in null width is obtained at the expense of higher gain ripple. The attenuator B controls the null width, but also has to be fixed at a suitable value to achieve an acceptable compromise between the null width and gain ripple.

Lim and Davies [41] proposed the use of two phase modes with a higher difference in order. This would have decreased the null width, but also would have lead to additional nulls in the radiation pattern. To avoid the additional nulls, the zero order mode was replaced with a beam pattern, which had a main beam of constant phase in the direction of the null. The beam pattern with a constant phase beam in the direction ϕ_p was obtained for a cylindrical array of omnidirectional elements by using the element excitations:

$$a_{n,beam} = e^{-jk_0R\cos\left(\phi_p - 2\pi\frac{n}{N}\right)}. \tag{2.35}$$

A sequence excitation, which was multiplied with a complex factor A, was added to the excitation of the constant phase beam to obtain a null in the direction ϕ_p. The factor A had to satisfy the following condition:

$$A \cdot F_m(\phi_p) + F_{beam}(\phi_p) = 0, \tag{2.36}$$

where $F_m(\phi_p)$ was the far-field radiation pattern of the sequence excitation of order m. The complex factor was found to be:

$$A = -\frac{N}{F_m(\phi_p)}, \tag{2.37}$$

and the resulting element excitations were:

$$a_n = e^{-jk_0R\cos\left(\phi_p - 2\pi\frac{n}{N}\right)} - \frac{N}{F_m(\phi_p)}e^{j\frac{2\pi mn}{N}}. \tag{2.38}$$

The sequence excitation in Equation 2.38 approximates a phase mode of the same order (m). Theoretically, an infinitely deep null with low gain ripple can be achieved. The gain ripple is determined by the interference of the phase mode with the sidelobes of the phase constant beam. The amount of interference is influenced by the number of elements, the array radius and the order of the phase mode. For a small number of

elements in the array, the order of the phase mode is usually low (zero or one). Larger arrays require a higher order phase mode to decrease the null width, which may result in an increased gain ripple. Therefore, the optimal order of the phase mode to be used, is determined by the radius of the array, the number of elements and the required ripple and null width.

2.3.3 Fourier approximation of an ideal pattern

The phase modes, which can be approximated by sequence excitations, form an orthogonal base for the array factor. A pattern can thus be synthesised by transforming the desired pattern into a number of phase modes with a Fourier transformation and then synthesising the phase modes with the sequence excitations. A Fourier transformation will however result in an infinite number of phase modes, but only the realisable orders of phase modes may be used to synthesise the pattern ($m \leq N/2$).

Lim [43] proposed the approximation of an ideal zero pattern using this method of approximation. For a minimum null width, an abrupt phase reversal in the pattern was needed in the direction of the null. To avoid the occurrence of a second null, the phase in the omniregion also had to change progressively at half the rate of the change in azimuth angle. An idealised pattern that satisfied these requirements was:

$$\begin{aligned} F_0(\phi) &= e^{j\frac{2\pi-\phi+\phi_p}{2}}, \\ \phi_p &\leq \phi \leq \phi_p + 2\pi. \end{aligned} \tag{2.39}$$

The phase of the pattern changes linearly from 0 (at $\phi = \phi_p$) to π (at $\phi = \phi_p + 2\pi$) and has an abrupt phase reversal at ϕ_p, as shown in Figure 2.15 for $phi_p = 180°$.

The approximation of the amplitude pattern of $F_0(\phi)$ will result in a null of finite depth, because the realisable pattern is limited in bandwidth and the derivations, with respect to ϕ, also have to be smooth. Using the standard method for calculating Fourier coefficients, the set of phase modes can be determined as:

$$\begin{aligned} p_m &= \frac{1}{2\pi} \int_{\phi_p}^{\phi_p+2\pi} F_0(\phi)\, e^{-jm\phi} d\phi \\ &= \frac{e^{-jm\phi_p}}{\pi\left(m - \frac{1}{2}\right)}. \end{aligned} \tag{2.40}$$

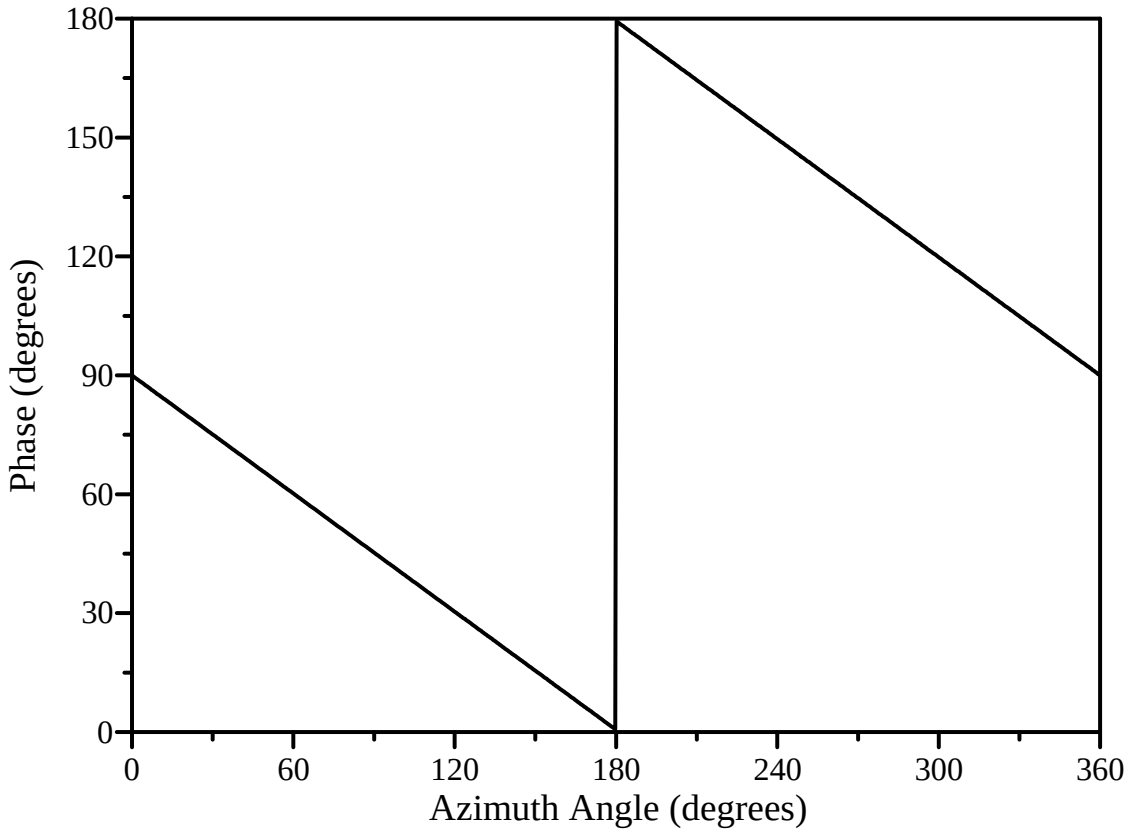

Figure 2.15: Phase of the idealised null pattern

For cylindrical arrays with identical elements and small inter-element spacings, the resulting sequence excitations will be:

$$s_m = \frac{e^{-jm\left(\frac{\pi}{2}+\phi_p\right)}}{\pi N \left(m-\frac{1}{2}\right) J_m(k_0 R)}, \tag{2.41}$$

where $J_m(x)$ is the Bessel function of the first kind of order m. The element excitations are obtained from the DFT relation in Equation 2.27.

The Fourier approximation will yield a pattern with a relatively narrow null, but with a gain ripple of about 2 dB. The realisable null depths are also low when a small number of elements are used. For small inter-element spacings ($< \lambda_0/4$) and radii, where the Bessel function $J_m(k_0 R)$ is not close to zero, the results appear to be insensitive to the array radius. For certain array radii, it will not be possible to create all the phase modes in the far field, if one or more Bessel functions $J_m(k_0 R)$ are very small or zero [43]. For the sequence excitations, where $J_m(k_0 R)$ is very small, the phase mode distortions in the far field pattern of these excitations will be much larger in amplitude than the wanted phase modes. The corresponding sequence excitations will be very large and

the distortion will dominate the far field, resulting in a large error of the approximation. Since the approximation is a superposition of phase modes, it will also lead to errors when the far field patterns, caused by the sequence excitations, are not exactly phase modes.

2.3.4 Orthogonal projection method

Instead of using the phase modes, the patterns g_m, caused by the sequence excitations, can be used as basis functions. These patterns are also mutually orthogonal and span the whole space of possible array patterns. Unlike the phase modes in the Fourier approximation, they can be synthesised exactly. The approximation will thus be better, especially when using larger inter-element spacings. Vescovo [50] applied this synthesis procedure to cylindrical arrays to synthesise beam patterns.

Every realisable array pattern, $F(\phi)$, of a cylindrical array with equally spaced antenna elements, can be written as the result of the sequence excitations s_m:

$$F(\phi) = \sum_{m=0}^{N-1} s_m g_m(\phi), \tag{2.42}$$

where

$$g_m(\phi) = \sum_{n=0}^{N-1} e^{j2\pi \frac{mn}{N}} E_n(\phi). \tag{2.43}$$

For a cylindrical array of equally spaced elements, the $g_m(\phi)$ of two different values of m are orthogonal to each other. A complete orthogonal base for the space of realisable array patterns is thus given by $g_m(\phi)$. For a cylindrical array of omnidirectional elements $g_m(\phi)$ is given by:

$$g_m(\phi) = \sum_{n=0}^{N-1} e^{j2\pi \frac{mn}{N}} e^{jk_0 R \cos\left(\phi - \frac{2\pi n}{N}\right)}. \tag{2.44}$$

The unconstrained optimal array pattern $F_{optim}(\phi)$ is the orthogonal projection of the idealised pattern $F_0(\phi)$ onto the space of realisable array patterns, when $F_{optim}(\phi)$ gives the minimum squared distance between $F(\phi)$ and $F_0(\phi)$. The squared distance $\rho^2(\mathbf{A})$ is defined as:

$$\rho^2(\mathbf{A}) = \int_0^{2\pi} |F(\phi; \mathbf{A}) - F_0(\phi)|^2 \, d\phi, \tag{2.45}$$

where $F(\phi; \mathbf{A})$ denotes the array radiation pattern for the excitation vector $\mathbf{A}$. The unconstrained optimum sequence excitations are thus obtained through the orthogonal projection [50]:

$$s_{optim\_m} = \frac{\langle F_0(\phi), g_m(\phi) \rangle}{\|g_m(\phi)\|^2}, \tag{2.46}$$

with the scalar product given by:

$$\langle f, g \rangle = \int_0^{2\pi} f(\phi) g(\phi) d\phi, \tag{2.47}$$

and the norm obtained from:

$$\|f\| = \sqrt{\langle f, f \rangle}. \tag{2.48}$$

The idealised radiation pattern $F_0(\phi)$ of [43] in Equation 2.39, may be used in the projection method to form a null in an otherwise omnidirectional array pattern. This null synthesis technique was proposed by Abele *et al* [53, 54]. The pattern $F_0(\phi)$ is projected onto the space of realisable array patterns of a cylindrical array of omnidirectional elements, to obtain the sequence excitation. The element excitations are then obtained through the DFT relation.

When the inter-element spacing is small ($\ll \lambda_0/2$), the base functions $g_m(\phi)$ are good approximations of the phase modes of the pattern and consequently the results of the projection method and the Fourier approximation will be comparable. The projection method also takes into account the distortion of the phase modes and will therefore give better results than the Fourier approximation for larger inter-element spacings. Figures 2.16 and 2.17 respectively compare the amplitude and phase of the radiation patterns for a single null, using the Fourier approximation and orthogonal projection method. An array with 16 elements and a radius of λ_0 was used to form an infinitely deep null at 180°. Using this small inter-element spacing, the two methods yield similar results in both amplitude and phase. The amplitude and phase of the radiation patterns for the same null, using a larger inter-element spacing ($R = 1.385\lambda_0$), are shown in Figures 2.18 and 2.19, respectively. For this larger inter-element spacing, the orthogonal projection method produces a deeper null with less gain ripple. A smaller phase ripple is also observed in the phase pattern of the orthogonal projection method.

The gain ripple may be reduced by using window functions [53, 54]. The spectral components of the array pattern, which have to be multiplied with the window function,

are the phase modes. Since the sequence excitations and phase modes are related through a multiplication of a constant factor, the window function may be applied to the sequence excitations, instead of the phase modes.

Abele [54] proposed the application of a Hamming window of length N to the sequence excitations:

$$W_{HM}(k) = 0.54 + 0.46\cos\left(2\pi\frac{k}{N}\right). \tag{2.49}$$

The idealised pattern has a constant phase slope of a $\frac{1}{2}$ and therefore its Fourier components are symmetric to $k = \frac{1}{2}$. This symmetry may not be disturbed by the application of the window in order to maintain the linear phase change. The best results are thus obtained if the window is shifted and the m-th sequence excitation coefficient is multiplied by $W(m - \frac{1}{2})$. The window function may be applied to the sequence excitation coefficients of both the Fourier approximation and the orthogonal projection. The ripple is decreased using the window function, while the null width is increased. The null depth may also be significantly increased. As an example, an array with $N = 16$ and $R = \lambda_0$ was used to form a single null at 180°. The effects of the Hamming window on the amplitude and phase of the radiation patterns resulting from the orthogonal projection method, are shown in Figures 2.20 and 2.21, respectively. It is observed that although a deeper null with less ripple is formed, the null width is increased.

The idealised pattern can be extended to contain multiple phase reversals to achieve more than one null in an otherwise omnidirectional pattern. Abele proposed idealised patterns for an odd and even numbers of nulls. The phase reversals for an even number of nulls sum up to a total phase change of zero, while the phase reversals for an odd number of nulls give an overall phase change of ±180°. Hence, a linear phase change has to be introduced to a pattern with an odd number of nulls, while no phase is needed for an even number of nulls.

The null widths of the multiple nulls do not differ much from the null width of a single null if the angular spacing between the nulls are kept large enough. On the other hand, the ripple changes significantly as the ripple caused by the abrupt phase reversals are superimposed. The angular distances between the nulls determine if there will be an increase or decrease in the ripple between the nulls. The angular distance between two nulls may not be too small, otherwise one null will be formed between the nulls.

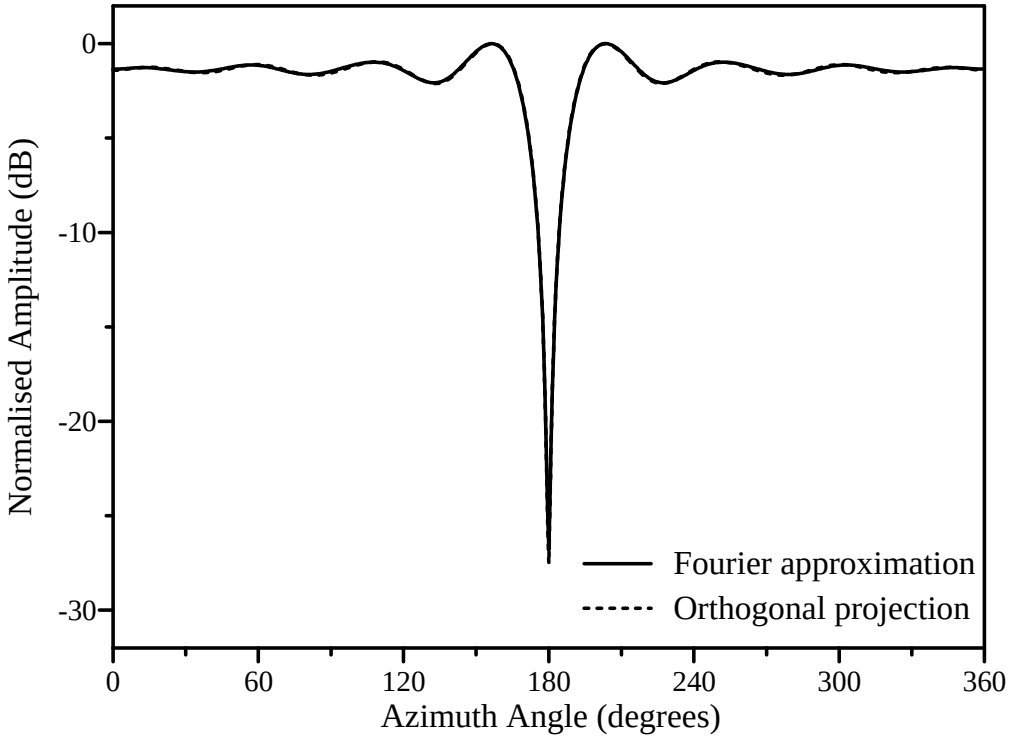

Figure 2.16: Comparison of the amplitude radiation patterns for a single null using the Fourier approximation and orthogonal projection (N=16 and $R = \lambda_0$)

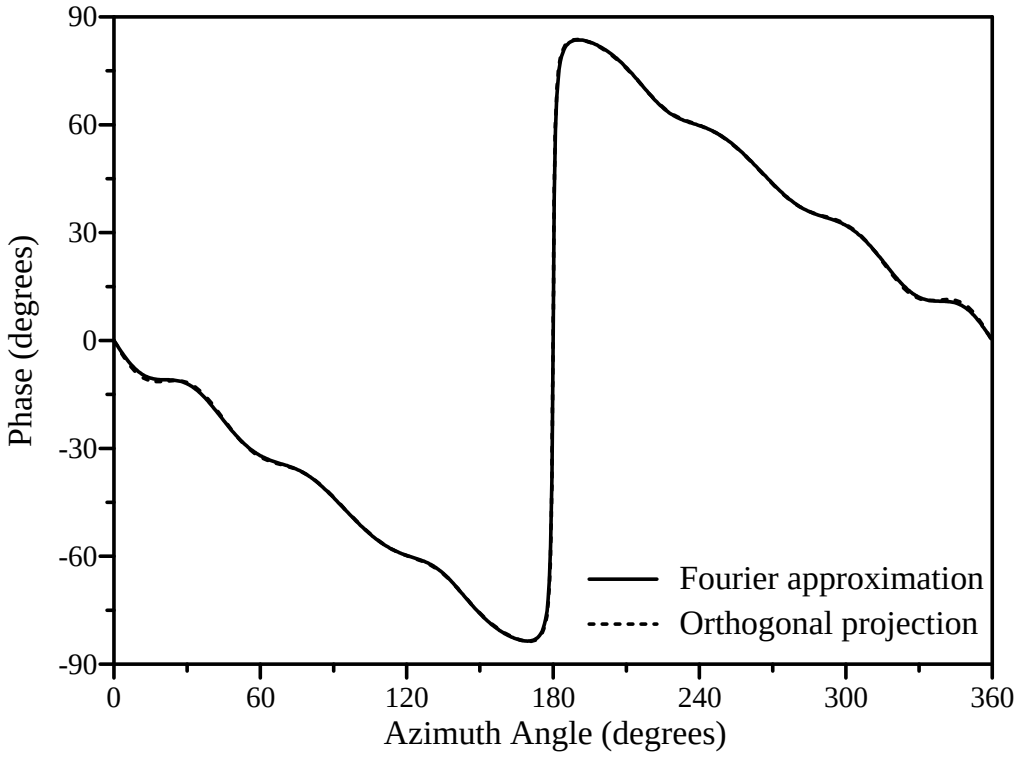

Figure 2.17: Comparison of the phase patterns for a single null using the Fourier approximation and orthogonal projection (N=16 and $R = \lambda_0$)

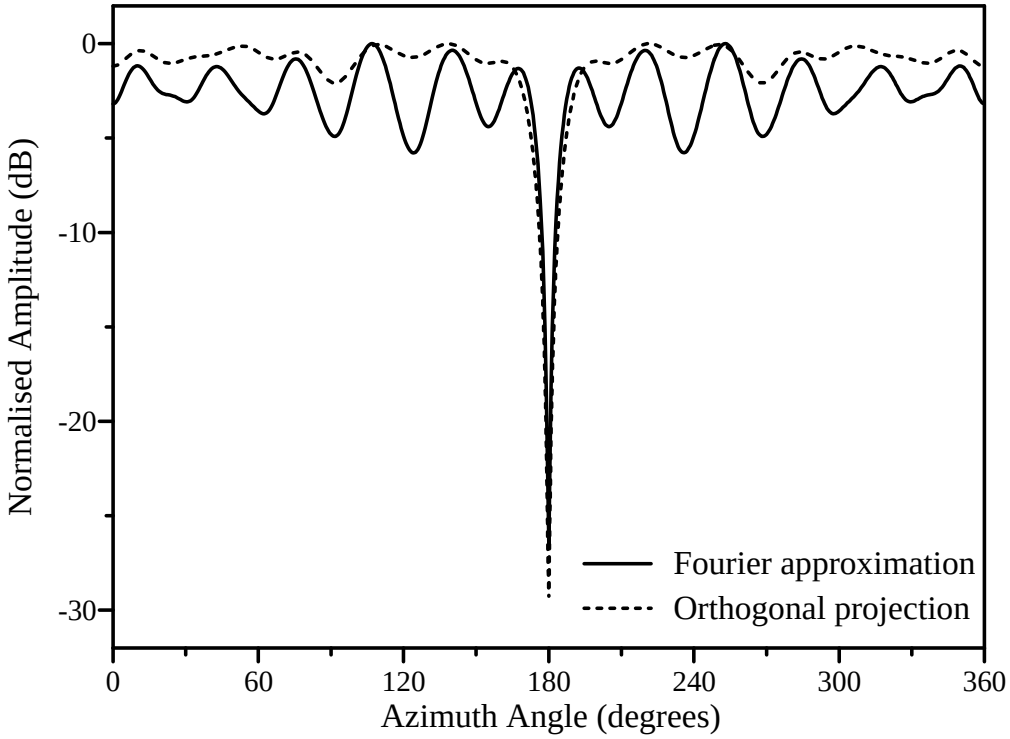

Figure 2.18: Comparison of the amplitude radiation patterns for a single null using the Fourier approximation and orthogonal projection (N=16 and $R = 1.385\lambda_0$)

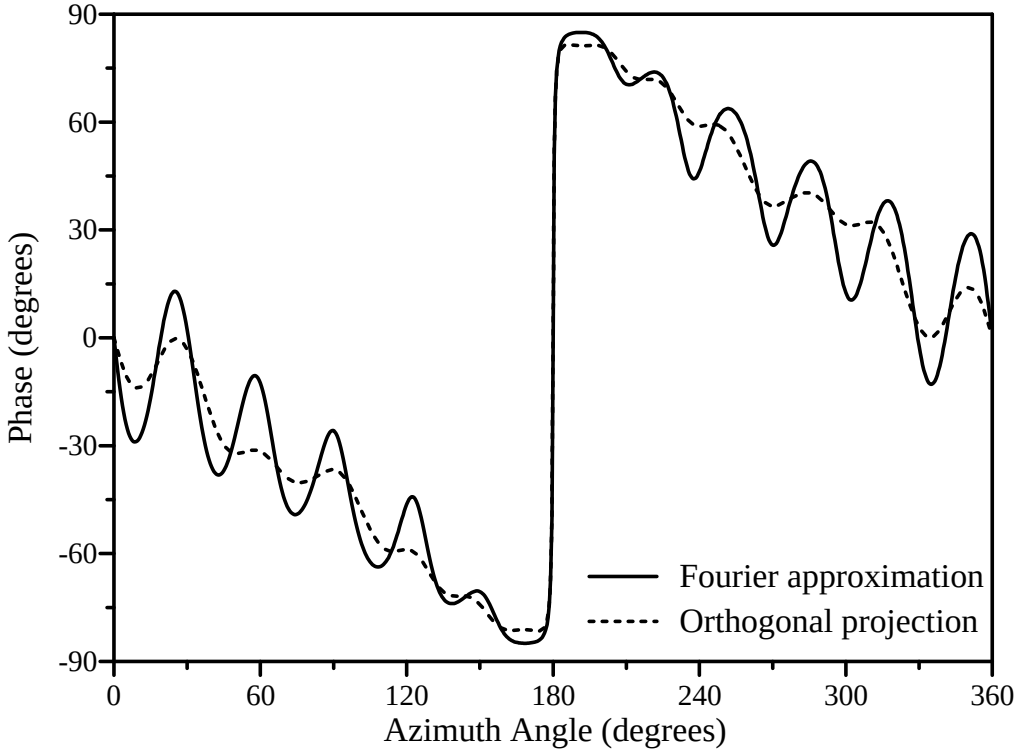

Figure 2.19: Comparison of the phase patterns for a single null using the Fourier approximation and orthogonal projection (N=16 and $R = 1.385\lambda_0$)

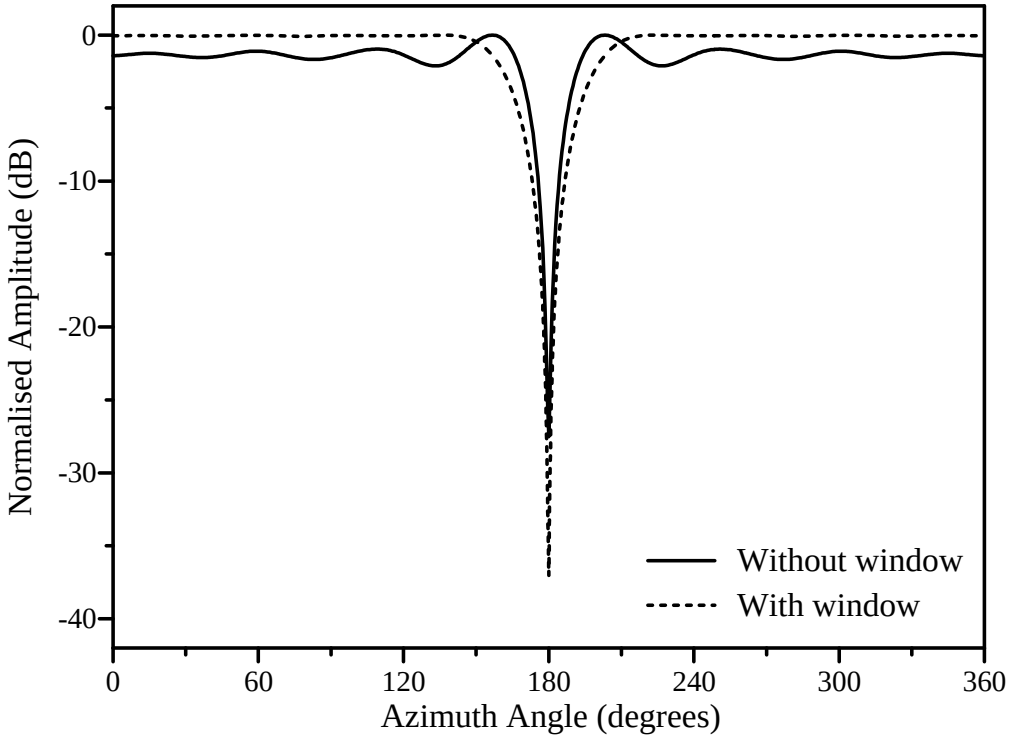

Figure 2.20: Comparison of the amplitude radiation patterns for a single null using the orthogonal projection method with and without a Hamming window (N=16 and $R = \lambda_0$)

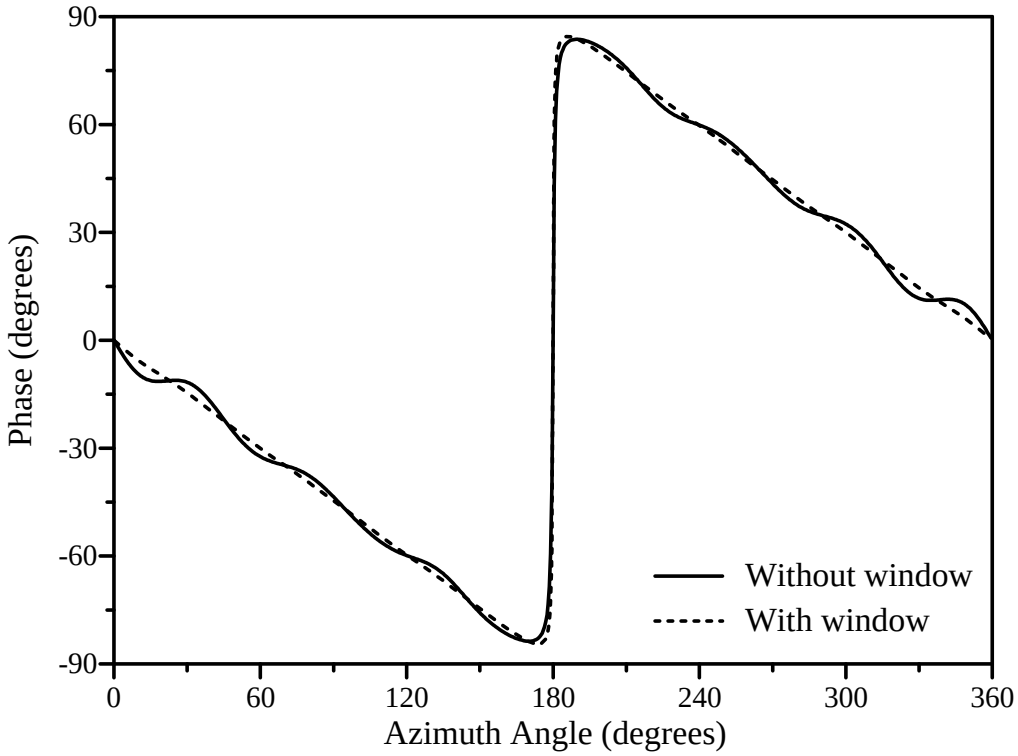

Figure 2.21: Comparison of the phase patterns for a single null using the orthogonal projection method with and without a Hamming window (N=16 and $R = \lambda_0$)

An omnidirectional pattern with two nulls at 90° and 270°, respectively, were simulated using the orthogonal projection method with a Hamming window. Figures 2.22 and 2.23 show the resulting amplitude and phase of the radiation pattern, respectively. An additional null was introduced at 180° and the amplitude and phase of the radiation pattern with three nulls are shown in Figures 2.24 and 2.25.

The difference in the phase patterns for odd and even nulls can be seen when Figures 2.23 and 2.25 are compared. A linear phase change is required for the introduction of the three nulls, whereas introduction of two nulls require no phase change. When comparing Figures 2.22 and 2.24, the effect of the spacing between the nulls on the null depths can also be seen. The null depths changed as the null spacing decreased from 180° to 90°.

Phase reversals of ±180° do not guarantee infinitely deep nulls. In general, the depths of the realised nulls depend on the array radius, the number of elements and the angular distance between the nulls. Abele [54] proposed the use of a variable phase step to provide control over the realised null depth. For a phase step of angle α, the absolute value of the average of both sides of the step will be:

$$\begin{aligned} \left|\hat{F}\right| &= \frac{|1+e^{j\alpha}|}{2} \\ &= \cos\frac{\alpha}{2}. \end{aligned} \tag{2.50}$$

If the desired null depth is expressed in dB relative to the maximum of the pattern, the required phase difference to achieve this null depth will be:

$$\alpha = 2\arccos\left(10^{\hat{F}_{dB}/20}\right). \tag{2.51}$$

The overall phase slope for a single null has to be $\alpha/2\pi$ to keep the pattern smooth in the omni-region. To introduce multiple nulls with specified null depths in the idealised pattern, the overall phase difference, after introducing the appropriate phase steps, has to be cancelled by a linear phase change. Therefore, the required phase slope of the idealised pattern for a number (L) of step angles α_l will be:

$$\nu = -\frac{1}{2\pi}\sum_{l=1}^{L}\Delta_l\alpha_l, \tag{2.52}$$

where Δ_l is the step direction of the phase step which may be equal to -1 or 1.

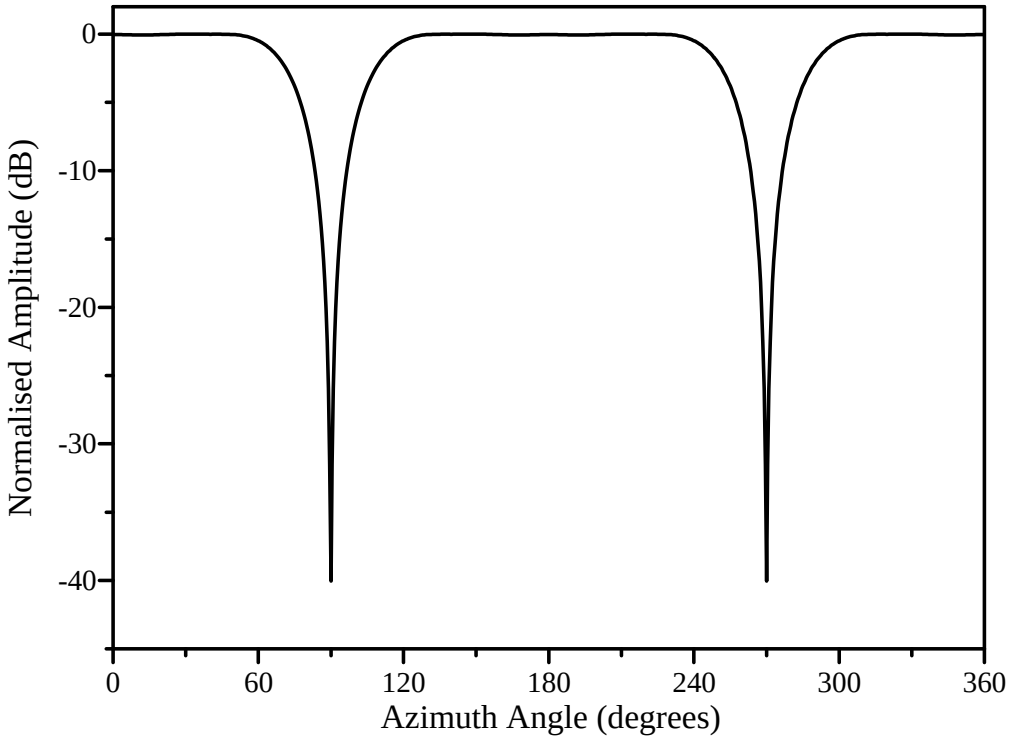

Figure 2.22: Amplitude radiation pattern for two nulls using the orthogonal projection method with a Hamming window (N=16 and $R = \lambda_0$)

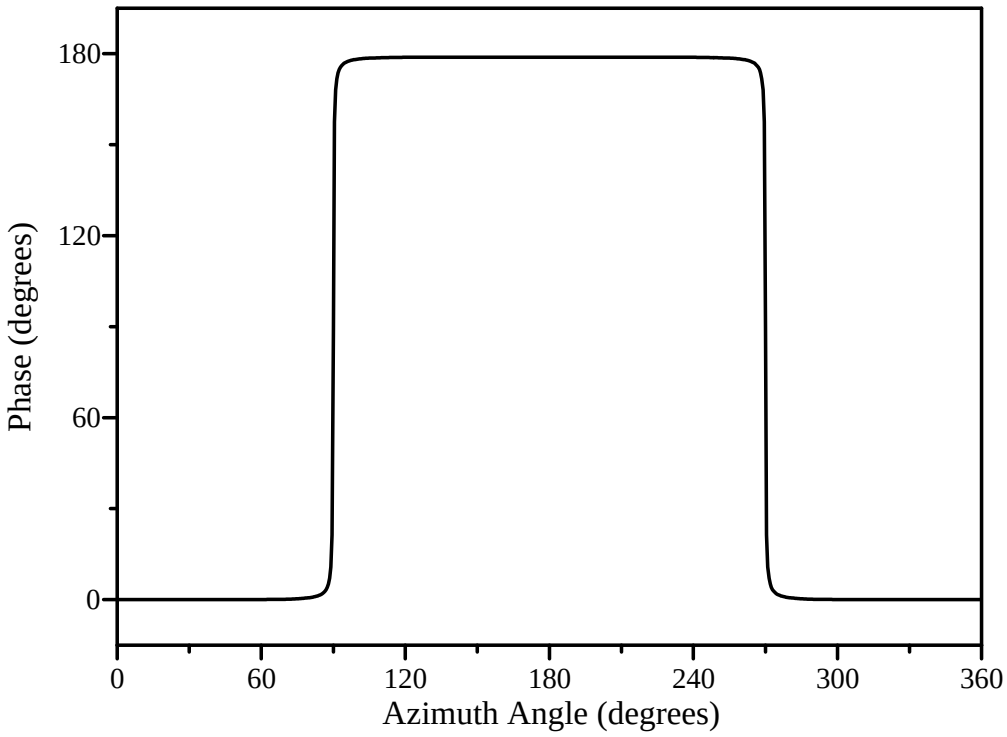

Figure 2.23: Phase pattern for two nulls using the orthogonal projection method with a Hamming window (N=16 and $R = \lambda_0$)

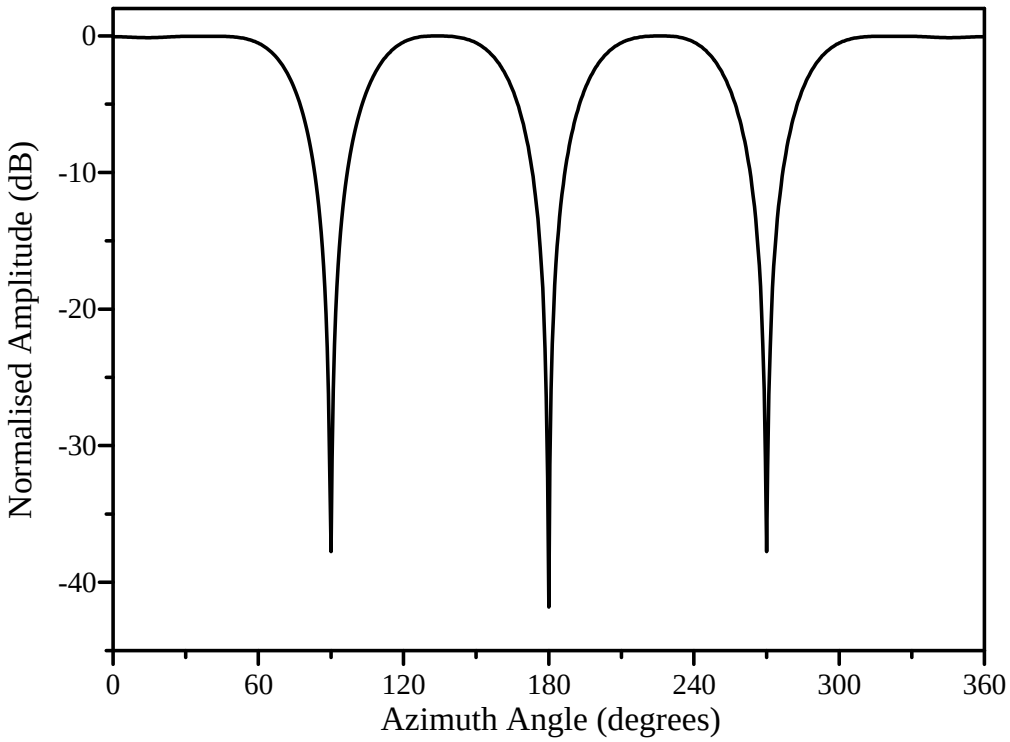

Figure 2.24: Amplitude radiation pattern for three nulls using the orthogonal projection method with a Hamming window (N=16 and $R = \lambda_0$)

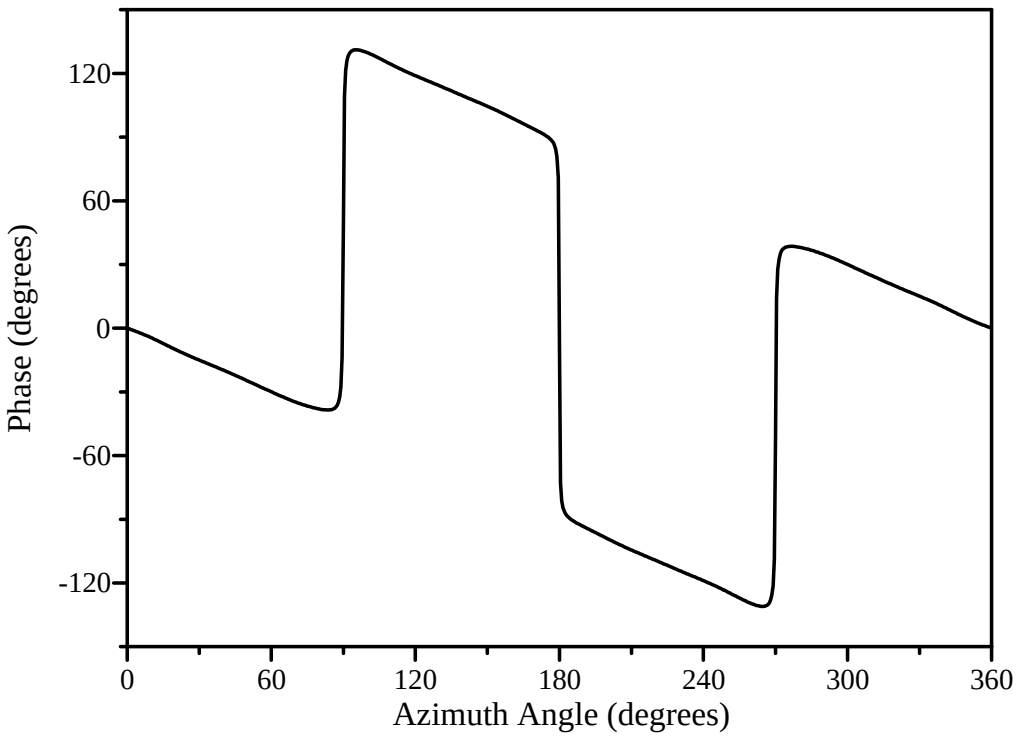

Figure 2.25: Phase pattern for three nulls using the orthogonal projection method with a Hamming window (N=16 and $R = \lambda_0$)

The directions of the phase steps are chosen in such a way as to minimise the sum of the phase differences and consequently minimise the required phase slope. If the previously mentioned windowing is required, the window displacement must be equal to ν. This method provides control over the null depths with acceptable accuracy, if the null depths are kept below 20 dB. Again the accuracy depends on the array configuration as well as the angular spacing between the nulls. The specified angular position of a null also has an influence on the null depth accuracy.

As an example, three nulls of depths 10 dB, 15 dB and 25 dB were required at 60°, 180° and 270°, respectively. The orthogonal projection, with a Hamming window, was utilised to form the desired nulls in the omnidirectional pattern of a 16 element array with a radius of λ_0. Figures 2.26 and 2.27 show the resulting amplitude and phase of the realised radiation pattern. The realised null depths are 9.9 dB, 15.1 dB and 24.1 dB at 60°, 180° and 270°, respectively. Each null depth requires a different phase step, as seen in the phase pattern in Figure 2.27. As the required null depth decreases, the null is also broadened.

2.3.5 Pattern synthesis with null constraints

When the radiation pattern is already given, Vescovo [50,51,55] proposed a method to introduce nulls into the pattern subsequently. The method was applied to reduce the sidelobe level by forming additional nulls near the main beam in a conventional beam pattern.

A radiation pattern, which does not necessarily satisfy the null constraint, is given by the N excitations a_n^0. The L null constraints, at the angles ϕ_l, are given by $F(\phi_l) = 0$ for $l = 1 \ldots L-1$.

The N excitations that minimise the Euclidean distance between the radiation pattern of a_n^0 and the pattern that satisfies the null constraint, are defined as a'_n. The squared Euclidean distance between the two patterns given by the sequence excitations s_m^0 and s'_m, is defined as:

$$\begin{aligned} \eta^2 &= \sum_{k=0}^{N-1} \left| b_m^0 - b'_m \right|^2 \\ &= \left\| \mathbf{b}^0 - \mathbf{b}' \right\|^2, \end{aligned} \tag{2.53}$$

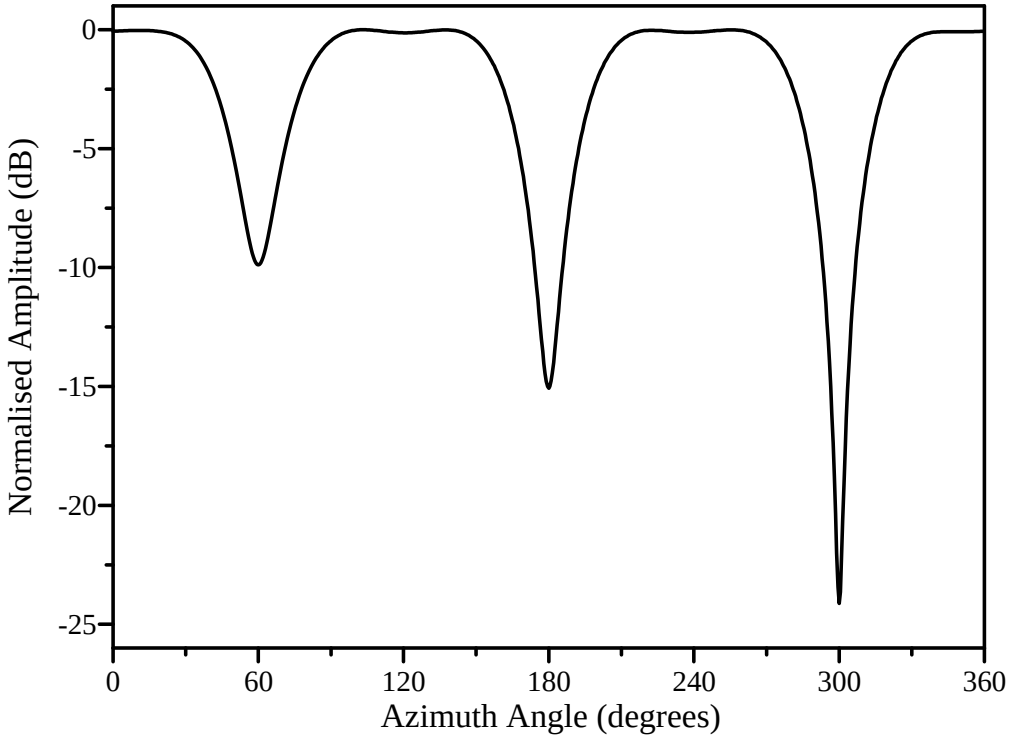

Figure 2.26: Amplitude radiation pattern of three nulls of required depths 10 dB, 15 dB and 25 dB at 60°,180° and 270°, respectively. (N=16 and $R = \lambda_0$)

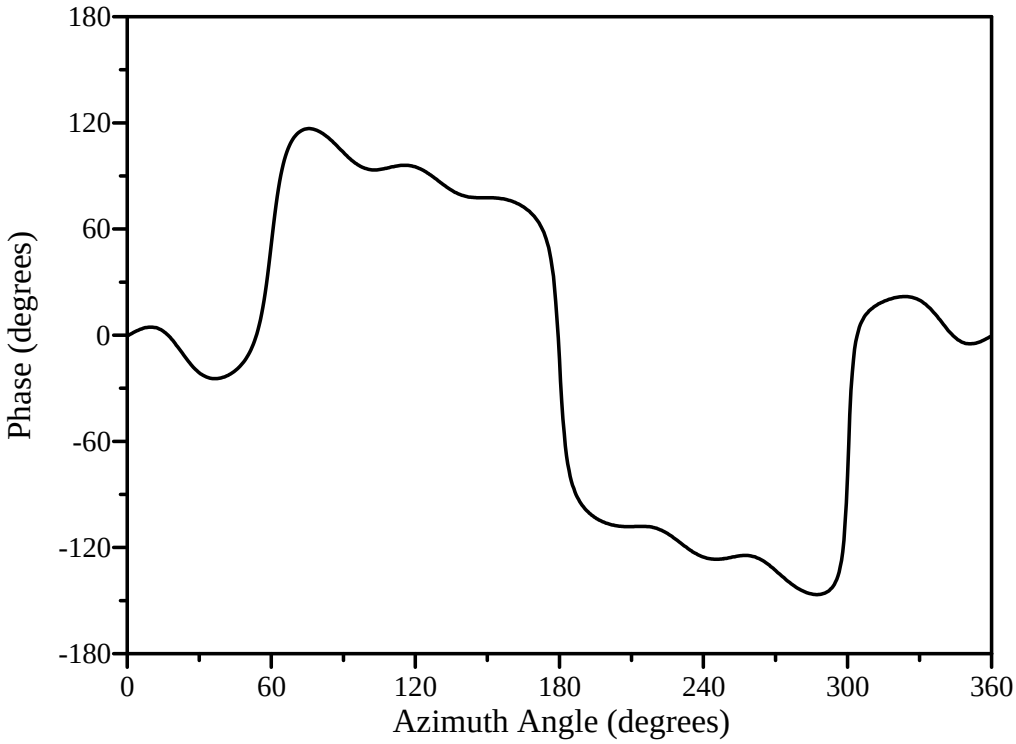

Figure 2.27: Phase pattern for three nulls of required depths 10 dB, 15 dB and 25 dB at 60°,180° and 270°, respectively. (N=16 and $R = \lambda_0$)

where

$$b_m^0 = \|g_m\| s_m^0 \tag{2.54}$$

and

$$b_m' = \|g_m\| s_m'. \tag{2.55}$$

Subsequently, the null constraints can be expressed as $\mathbf{B}\mathbf{b}' = 0$, where $\mathbf{B} = [B_{lm}]$ and $B_{lm} = g_m(\phi_l)/\|g_m\|$ for $l = 0 \ldots L-1$ and $m = 0 \ldots N-1$. The problem can therefore be described as minimising the Euclidian distance $\|\mathbf{b}^0 - \mathbf{b}'\|^2$ under the constraint $\mathbf{B}\mathbf{b}' = 0$. The optimal vector $\mathbf{b}'$ is given by [51]:

$$\mathbf{b}' = [\mathbf{I}_N - \mathbf{B}^H(\mathbf{B}\mathbf{B}^H)^{-1}\mathbf{B}]\mathbf{b}^0, \tag{2.56}$$

where $\mathbf{I}_N$ is a $N \times N$ identity matrix and $\mathbf{B}^H$ denotes the complex conjugate transpose of $\mathbf{B}$.

To obtain an omnidirectional pattern with nulls, the excitation vector $\mathbf{a}^0$ must be chosen in such a way as to yield an acceptable $\mathbf{a}'$. For the lowest possible ripple, $\mathbf{a}^0$ will be an excitation vector, which results in an omnidirectional pattern. The method produces infinitely deep nulls exactly at the desired angles, but with a gain ripple which can be as high as 20 dB.

Vescovo also proposed this technique to introduce nulls in the desired pattern of an arc array of directional elements [56]. Each directional element had a theoretical radiation pattern of:

$$E_n(\phi) = 1 + \cos(\phi - \phi_n). \tag{2.57}$$

Since the element radiation patterns point in different directions, the element pattern can not be factorised out of the array pattern to obtain an array factor [4,57]. Therefore, the orthogonal base defined in Equation 2.43 is used to obtain the desired pattern through the projection method. Additional nulls are formed afterwards by using null constraints.

2.3.6 Constrained minimisation with Lagrange multipliers

In this method, the distance between an idealised pattern and the realised pattern is also minimised [47]. As opposed to other methods, the idealised pattern has a constant phase and therefore the phase of the realised pattern will be almost constant. This

will result in an tangential null, where the phase is constant within the null and the resulting null width will consequently not be optimal. The squared error function:

$$\varepsilon^2 = \int_{-\pi}^{\pi} |AF(\phi) - 1| \, d\phi, \tag{2.58}$$

is minimised, subject to $AF(\phi_p) = 0$, where ϕ_p is the angle position of the null. The squared error is minimised using the method of Lagrange multipliers, which result in the vector of element excitations:

$$\mathbf{a} = \mathbf{Q}^{-1} \left[\mathbf{p} - \frac{\mathbf{d}^H(\phi_p)\mathbf{Q}^{-1}\mathbf{p}}{\mathbf{d}(\phi_p)\mathbf{Q}^{-1}\mathbf{d}(\phi_p)} \mathbf{d}(\phi_p) \right], \tag{2.59}$$

where $\mathbf{Q}$ is an $N \times N$ matrix with elements:

$$Q_{ij} = J_0 \left(2k_0 R \sin \left(\frac{\pi}{N} |i - j| \right) \right). \tag{2.60}$$

The N-dimensional vectors $\mathbf{d}(\phi)$ and $\mathbf{p}$ have elements:

$$d_i(\phi) = e^{jk_0 R \cos\left(\phi - \frac{2\pi}{N}\right)}, \tag{2.61}$$

and

$$p_i(\phi) = J_0(k_0 R), \tag{2.62}$$

respectively.

The realised pattern of this method has an infinitely deep null exactly at the desired location of the null. The tangential null is wider than the zero-crossing null and show a gain ripple between 2.5 and 3.5 dB. The constant idealised phase appears not to be suitable for the synthesis of an omnidirectional pattern with a narrow null and low gain ripple.

2.3.7 Constrained optimisation techniques

The methods, which have been discussed in the previous sections, all provide an omnidirectional pattern with nulls, but with different null depths, null widths and gain ripples. These methods do not have the ability to constrain a certain property of the array pattern.

Constrained optimisation allows the prescription of some of the characteristics of the array pattern, while optimising the others. The null width, for example, may be optimised for a given gain ripple and null depth, or the gain ripple may be minimised, while specifying the null width and null depth values. An optimisation technique may also allow the definition of any criteria relevant to the specified application e.g. allowable excitation amplitudes and phases.

These optimisation techniques may utilise methods such as the least squares optimisation method [45], the minimax and linear programming methods [48], the Hooke and Jeeves algorithm [45] and the simulated annealing method [52]. Prasad [45] applied the least squares optimisation method to circular and arc arrays to form a beam pattern with a specified beamwidth. Additional nulls were also placed in the sidelobe region by using null constraints while minimising the mean square difference between the desired pattern and the optimum pattern. The Hook and Jeeves algorithm was also used to perform an iterative search to find the optimum excitation vector while satisfying the null constraints. During the search, the sidelobe level was minimised.

For linear arrays, Mismar [48] introduced a method to locate nulls in the prescribed directions while keeping the main beam towards the desired signal. A minimax approximation technique is used to search for the maximum point in the constraint region to control the sidelobe level directly, while at the same time control the main beam characteristics as required. Ares *et al.* [52] used a simulated annealing technique to produce beam patterns for a circular arc array on a cylinder. A cost function, which could include terms to control the radiation pattern, was minimised. Terms which placed constraints on the excitations, could also be included in the cost function.

Since the desired pattern is a function of the excitation vector, the search is executed in a $2N$-dimensional space. A high computational expense is thus encountered. The choice of the starting values also plays a very important roll in the success of these pattern search techniques. Choosing the starting values carefully can limit the computational time and avoid local minima. The use of an excitation vector, with a resulting pattern error close to the global minimum, is encouraged.

2.4 Mutual coupling compensation

If the element excitations, obtained from the null synthesis technique, are applied to the antenna elements, distortion of these excitations may occur due to the mutual coupling between the antenna elements in the array. The consequent errors in the element excitations deteriorate the desired radiation pattern [72, 73]. Therefore, the mutual coupling must be compensated for to avoid errors in the desired characteristics of the null.

Lo [74] investigated the effect of the mutual coupling on the beam scanning and null steering performance of a linear monopole array. It was found that null filling and/or null steering errors occurred when the mutual coupling was not compensated for during the computation of the element excitations. The effect of the mutual coupling on the null pattern of a cylindrical dipole array was studied by Abele *et al.* [54]. The mutual coupling between the dipoles had a deforming effect on the the null pattern. Null filling and null position errors also occurred and the gain ripple was increased.

One direct way of minimising the effect of the mutual coupling, is by reducing the mutual coupling itself. The antenna elements in the array, for example, can be designed in such a way as to exhibit small coupling values. Absorbing material can be placed between the elements to reduce the coupling or the spacing between the elements can be chosen in such a way, that the coupling has an insignificant effect on the desired radiation pattern.

Another way of dealing with the coupling, is to compensate for it in the pattern synthesis technique. Impedance and coupling matrixes are used in the pattern synthesis technique to compute corrected element excitations, which compensate for the mutual coupling. According to Ghorbani [87], the mutual coupling also causes a mismatch between the driving impedances of the antenna elements and the feeding system of the array. This effect may significantly degrade the performance of narrowband arrays. These driving impedances can be corrected by altering the physical properties of the antenna elements to obtain the desired driving impedances for a required set of element excitations. A short overview of these techniques is given in the following sections.

2.4.1 Minimising the mutual coupling effects

Lo and Vu [74] investigated the use of guard elements in a linear monopole array to reduce the effect of the mutual coupling on null steering. Due to mutual coupling, the active element patterns are not comparable, which result in null filling and null steering errors. It was found that by placing guard elements at both ends of the linear array, the active element patterns resemble each other more closely. The perturbation of the zeros is reduced and consequently the null filling and null steering error are minimised. The method does not completely compensate for the mutual coupling, but is able to minimise the coupling effect without changing the element excitations.

When computing the coupling between array elements, the coupling of the electromagnetic fields in the free space immediately above the elements, is usually considered in the calculation. For microstrip array elements constructed on the same common substrate, additional coupling occurs due to the surface wave in the substrate. When using thick substrates, this surface wave coupling can be very strong due to a larger surface wave being generated. Bamford *et al* [81] examined the direct radiation and surface wave coupling separately through a method based on the reaction theorem. The behaviour of the total coupling was also studied for various element separation distances and substrate thicknesses. It was found that when the two coupling parameters are in phase, they add to form an upper limit curve for the coupling, but also form a lower limit curve when they are opposite in phase. A reduction in mutual coupling is thus possible through an appropriate choice of substrate thickness and separation distance between the array elements. The possible heights for the substrate are usually determined by the required bandwidth and the available substrate thicknesses as supplied by the manufacturers. Similarly, the possible separation distances are limited by the desired radiation pattern characteristics. Therefore, the reduction of the mutual coupling using this method may be limited by the requirements on the impedance and radiation behaviour of the array.

2.4.2 Compensation using coupling and impedance matrixes

Steyskal and Herd [76] showed that the element excitations a_n can always be chosen in such a way as to compensate for the pattern error due to mutual coupling. The technique uses the formulation that any composite array pattern is a weighted sum

of the isolated element patterns and that the mutual coupling parasitically excites all the elements. The mutual coupling can thus be compensated for by driving the array with modified element excitations in such a way that the desired radiation pattern is obtained in the presence of these parasitics. The coupling perturbed signals and the unperturbed desired signals, can be related through a coupling matrix $\mathbf{C}$:

$$\mathbf{v} = \mathbf{C}\mathbf{v^d}, \tag{2.63}$$

where the vectors $\mathbf{v}$ and $\mathbf{v_d}$ represent the coupling perturbed signals v_n and the desired signals v_n^d, respectively. The compensation for the mutual coupling can thus be accomplished by simply multiplying the received signals $\mathbf{v}$ with the inverse of the coupling matrix:

$$\mathbf{v^d} = \mathbf{C^{-1}}\mathbf{v}. \tag{2.64}$$

This method restores the signals as being received by the isolated antenna elements in the absence of coupling. The coupling coefficients can be obtained from two different methods: a Fourier decomposition of the measured element patterns or coupling measurements between the array ports. The matrix $\mathbf{C^{-1}}$ may be very difficult or impractical to realise with an analog network, but can be easily realised in a digital beam forming antenna system. Darwood *et al* also extended this technique for planar arrays [82]. The method assumes that the current distribution over the array elements is not affected by the coupling and remains unchanged from one element to the other in the array. It is furthermore assumed that only the input impedance of the element is affected by the mutual coupling. This approach may fail when electrically large elements and arrays of dissimilar elements are considered.

Any errors in the coupling matrix, due to these assumptions, will contribute to the degradation of difference beam patterns. Fletcher *et al* [80] derived a covariance matrix for any signal direction of arrival that includes the effects of the mutual coupling. By multiplying the inverse of this covariance matrix with the coupling corrected difference beam excitation vector, an optimum excitation vector is found which restores the difference beam pattern.

Derneryd [79] proposed an alternative way of viewing the matrix multiplication technique. An array antenna can be represented by a multiport network that is characterised by a $N \times N$ scattering matrix, $\mathbf{S}$ [75]. This scattering matrix relates the forward

and backward travelling waves, $\mathbf{v}^+$ and $\mathbf{v}^-$, respectively, on the feed lines:

$$\mathbf{v}^- = \mathbf{S}\mathbf{v}^+. \tag{2.65}$$

The array excitation vector $\mathbf{A}$ is given by the sum of the incident and reflected signals and in the transmitting mode it becomes:

$$\begin{aligned} \mathbf{A} &= \mathbf{v}^+ + \mathbf{v}^- \\ &= (\mathbf{I} + \mathbf{S})\mathbf{v}^+ \\ &= \mathbf{C}\mathbf{v}^+, \end{aligned} \tag{2.66}$$

where I is the unit matrix. The modified incident signals to produce the desired radiation pattern in the mutually coupled environment, is thus given by:

$$\mathbf{v}^+ = \mathbf{C}^{-\mathbf{1}}\mathbf{v}^{\mathbf{d}}. \tag{2.67}$$

These modified signals can be controlled by amplifiers and phase shifters.

The inclusion of the mutual coupling in the relation of the incident and reflected waves is also applied by Eclercy *et al* [72, 77], though in this method the effect of the mutual coupling is taken into account in the radiated field of the array. The reflection coefficient at the feed line of the n-th antenna element is defined as:

$$\Gamma_n = \frac{v_n^-}{v_n^+}, \tag{2.68}$$

where

$$v_n^- = \sum_{p=1}^{N} S_{np} v_p^+. \tag{2.69}$$

Keeping the mutual coupling in mind, the radiation pattern can be written as:

$$\begin{aligned} F(\phi) &= \sum_{n=1}^{N} E_n(\phi)(v_n^+ + v_n^-)e^{jk_0(x_n\cos\phi + y_n\sin\phi)} \\ &= \sum_{n=1}^{N} E_n(\phi)v_n^+(1+\Gamma_n)e^{jk_0(x_n\cos\phi + y_n\sin\phi)}. \end{aligned} \tag{2.70}$$

This radiation pattern is then used in the pattern synthesis method to obtain the modified element excitations, which compensate for the mutual coupling.

Using the vector notation of Equation 2.18, the array radiation pattern can be written as [83]:

$$\begin{aligned} \mathbf{F} &= \mathbf{B}(\mathbf{I} + \mathbf{S})\mathbf{v}^{+} \\ &= \mathbf{B}'\mathbf{v}^{+}, \end{aligned} \tag{2.71}$$

where $\mathbf{A}$ is replaced using Equation 2.66. The matrix $\mathbf{B}'$ and the pattern $\mathbf{F}$ are computed at more angles than there are elements in the array. The solution for $\mathbf{v}^{+}$ is thus obtained in a least squares sense. This method assumes that the element patterns are all equal to the element pattern of an isolated element. Where antenna elements are closely spaced, the current distributions of the elements are changed by the coupling, resulting in active element patterns. Taking this into consideration, Caccavale *et al* [85] proposed an active element convex programming method (ACE-COP), in which the array radiation pattern is expressed as the superposition of active element patterns. The method is mostly applicable to small arrays, due to the additional computational burden required by the evaluation of the active element patterns. In large arrays, where most of the elements experience similar electromagnetic environments, it can be assumed that all the elements radiate the same active element pattern. This approach is referred to as the modified element pattern (m.e.p.) technique [85].

The correction for the mutual coupling may also be done through the impedance [54, 78,85] or admittance [84] relations between the antenna element currents and voltages. If the currents of the antenna elements are set proportional to the computed excitation coefficients, the driving voltages of the elements can be expressed as:

$$\mathbf{V} = \mathbf{Z}\mathbf{I}, \tag{2.72}$$

with $\mathbf{V}$ and $\mathbf{I}$ being $1 \times N$ the driving voltage and current vectors, respectively, and $\mathbf{Z}$ being a $N \times N$ impedance matrix. The driving voltage of the m-th element, that compensates for the mutual coupling with the other antenna elements, can thus be

written as:

$$\begin{aligned} V_m &= \sum_{n=1}^{N} Z_{mn} I_n \\ &= Z^s_{mm} I_m + \sum_{\substack{n=1 \\ n \neq m}}^{N} Z_{mn} I_n, \end{aligned} \tag{2.73}$$

where Z^s_{mm} is the self impedance of the m-th antenna element and Z_{mn} is the mutual impedance between the m-th and n-th antenna elements. The self and mutual impedances depend on the type of antenna elements as well as the mounting structure used to construct the array. Abele *et al* [54] introduced a variable:

$$Z_n = \begin{cases} Z^s_{nn} & \text{for } n \bmod N = 0, \\ Z_{1,n \bmod N} & \text{for } n \bmod N \neq 0, \end{cases} \tag{2.74}$$

for $n = 1 \ldots N$. Equation 2.73 can then be written as:

$$\begin{aligned} V_m &= \sum_{n=1}^{N} Z_{m-n} I_n \\ &= \{Z_n; n = 1 \ldots N\} * \{I_n; n = 1 \ldots N\}, \end{aligned} \tag{2.75}$$

where the asterisk denotes a circular convolution.

The correction for the mutual coupling can be included in the design procedure by multiplying the desired sequence excitation coefficients with the DFT of the impedances Z_n, before computing the element excitations a_n. The element currents and driving voltages are then defined as:

$$I_n = I_0 \cdot \text{IDFT}\{s_m; m = 1 \ldots N\}, \tag{2.76}$$

and

$$V_n = I_0 \cdot \text{IDFT}(\text{DFT}\{Z_n; n = 1 \ldots N\} \cdot \{s_m; m = 1 \ldots N\}). \tag{2.77}$$

When setting the element voltages proportional to the excitation coefficient, similar expressions can be found for the necessary driving currents, using the admittance relation:

$$\mathbf{I} = \mathbf{Y}\mathbf{V}. \tag{2.78}$$

The driving current of the m-th element may also be written as:

$$\begin{aligned} I_m &= \sum_{n=1}^{N} Y_{mn} V_n \\ &= Y^s_{mm} V_m + \sum_{\substack{n=1 \\ n \neq m}}^{N} Y_{mn} V_n, \end{aligned} \tag{2.79}$$

with Y^s_{mm} and Y_{mn} respectively denoting the self admittance of the m-th element and mutual admittance between the m-th and n-th elements.

2.4.3 Modification of the driving impedances

From Equation 2.73, the driving impedance of the m-th element can be expressed as:

$$Z^a_m = Z^s_{mm} + \sum_{\substack{n=1 \\ n \neq m}}^{N} Z_{mn} \frac{I_n}{I_m}. \tag{2.80}$$

It is observed that the driving impedances do not only depend on the configurations of the array and the antenna elements, but also on the currents of the elements. When designing the feed network of the array, it is these driving impedances which have to be matched. If the mismatches at the feed ports are not taken into account, it may significantly degrade the performance of narrowband arrays. The resulting driving impedances obtained from the radiation pattern correction methods remain unmatched and unequal. Consequently, the design of a feeding and matching network can be complicated.

Another possibility is to alter the individual element geometries physically in order to have equal driving impedances for the required element excitations [86, 88, 89]. Yang *et al* [86] proposed this technique for an electromagnetically coupled (EMC) dipole antenna array. From Equation 2.79, the driving admittance of each element in the array can be obtained as:

$$Y^a_m = Y^s_{mm} + \sum_{\substack{n=1 \\ n \neq m}}^{N} Y_{mn} \frac{V_n}{V_m}. \tag{2.81}$$

In a linear system, a second design equation can be derived from the current in each dipole:

$$\frac{I_m^a}{V_m} = \frac{I_{mm}}{V_m} + \sum_{\substack{n=1 \\ n \neq m}}^{N} \frac{I_{mn}}{V_n}, \tag{2.82}$$

where I_{mm} is the current of the m-th dipole in the absence of other dipole and I_{mn} is the current of the m-th dipole due to the current on the n-th dipole. The admittances and currents are functions of the voltages, dipole lengths and dipole offsets from the microstrip feed line. For a given design goal, e.g. the active currents on the dipoles, a set of dipole lengths and offsets is found, which not only satisfies Equation 2.82, but also provides the prescribed driving admittances seen by the feed lines. Design curves for the mutual admittances and self admittances are obtained from a method of moments solution. A desired bandwidth and voltage standing wave ratio (VSWR) at the resonant frequency are obtainable, while finding good agreement between the desired and measured radiation patterns.

Chen *et al* proposed a similar technique for a linear array of parallel dipoles [88]. In this case, the lengths and the radii of the dipoles were changed to obtain the desired radiation pattern as well as equal driving impedances for the dipoles. This resulted in a feed network that was much simpler than usual. The technique was also extended to planar dipole arrays [89]. Input impedances of 75Ω for the dipoles, as well as the required radiation pattern, were obtained.

2.5 Summary

Different characteristics of the cylindrical microstrip patch antenna have been discussed. The cavity model was used to illustrate the influence of some of the design parameters of the cylinder and the patch antenna on the radiated element pattern. Therefore the design of the antenna element, has an influence on the characteristics of the total radiated array pattern. Since the radiation characteristics of the cylindrical patch antenna also depend on the polarisation, the choice of polarisation must be included in the design procedure of the array pattern.

The radiated array pattern of a cylindrical array has also been discussed. Equally spaced cylindrical arrays have the unique characteristic that they can produce omni-

directional patterns by being excited with phase-sequence excitations. A combination of these sequence excitations can be used to form a desired array radiation pattern. The element excitations are obtained from the resulting coefficients of the sequence excitations through a discrete Fourier transform.

An omnidirectional radiation pattern, with nulls at the specified angle directions, is defined as the desired radiation pattern. An overview of null synthesis techniques was given to obtain this desired radiation pattern with cylindrical arrays. The superposition of sequence excitations is only suitable for arrays with a small number of elements, while the Fourier approximation perform well only for small inter-element spacings. When null constraints are used to form the nulls, the resulting ripple is very high. The increased null width is the main drawback of constraint minimisation with Lagrange multipliers. The orthogonal projection method and its extensions are well suited to form the desired radiation pattern for most cylindrical array configurations. Some control over the null depths and ripple are provided through variable phase steps and a window function. Pattern optimisation techniques can be used to obtain the desired pattern, while optimising certain array pattern characteristics. In Chapter 3, the orthogonal projection method is extended for a cylindrical microstrip patch array to provide an omnidirectional pattern with one or more nulls. The resulting excitation vector is also used as the starting value for two optimisation algorithm, which allows the specification and/or optimisation of certain pattern characteristics, e.g. null depth, null width and gain ripple.

The synthesis of the radiation pattern is influenced by the mutual coupling between the antenna elements. If the mutual coupling is not compensated for in the design procedure, the consequent errors in the element excitations may deteriorate the radiation pattern. Minimisation of the coupling reduces the effect of the coupling on the radiation pattern, but does not totally compensate for the coupling. By using a coupling or impedance matrix to include the mutual coupling in the design procedure, the coupling is completely compensated for. However, the driving impedances remain unmatched and may result in complicated feed networks. As an alternative, the geometries of the elements may be varied to provide matched and equal driving impedances for all the antenna elements, given a required set of element excitations. This compensation technique is applied to the cylindrical patch array in Chapter 4 by altering the geometries of the patch antenna elements. This technique provides the desired pattern by correcting the driving impedances.